Improved joint prediction strategy for state of charge and peak power of lithium-ion batteries by considering hysteresis characteristics-current measurement deviation correction.

QI, C., WANG, S., CAO, W., WANG, Y., LIU, D. and FERNANDEZ, C.

2024

Journal of Energy Storage

Improved Joint Prediction Strategy for State of Charge and Peak Power of Lithium-ion Batteries by Considering Hysteresis Characteristics-Current Measurement Deviation Correction

--Manuscript Draft--

Abstract:	The peak power and state of charge of lithium-ion batteries are closely related to the safety of electric vehicles. Accurate peak power and state of charge prediction can extend battery life while ensuring safe driving. In this paper, a modeling strategy for the joint estimation of the battery state of charge and peak power is proposed to consider the effect of current measurement deviation. First, a modified Thevenin model of the battery considering the internal polarization reaction process and the open-circuit voltage hysteresis effect is developed to improve the physical significance of the parameter identification results. On this basis, a current measurement deviation correction strategy based on the double-layer forgetting factor recursive least squares algorithm is proposed. To solve the nonlinearity and noise disturbance problems of the battery system, an unscented Kalman filter-based multi-parameter constrained adaptive dynamic state observer is developed and used for the joint estimation of the state of charge and peak power. In particular, multiple parameters such as current, voltage, and state of charge are selected for the prediction of the battery peak power. Experimental results for different complex dynamic conditions at different temperatures show the excellent performance of the proposed modeling method in predicting the validity and accuracy verification of the state of charge and peak power. The proposed method provides a viable theoretical basis for the manufacturing technology of advanced battery management systems.

1. A high-fidelity Thevenin model that takes into account battery polarization and hysteresis phenomena is established.
2. A current measurement deviation correction strategy based on double-layer forgetting factor recursive least squares algorithm is proposed.
3. An multi-parameter constrained adaptive dynamic state observer for joint SOC and peak power prediction is proposed.

Improved Joint Prediction Strategy for State of Charge and Peak Power of Lithium-ion Batteries by Considering Hysteresis Characteristics-Current Measurement Deviation Correction

Chuangshi Qi [a], Shunli Wang [a,b]*, Wen Cao [a], Yangtao Wang [a], Donglei Liu [a], Carlos Fernandez [c]

[a] *School of Information Engineering, Southwest University of Science and Technology, Mianyang 621010, Sichuan, China*

[b] *College of Electrical Engineering, Sichuan University, Chengdu 610065, China*

[c] *School of Pharmacy and Life Sciences, Robert Gordon University, Aberdeen AB10-7GJ, UK*

Abstract: The peak power and state of charge of lithium-ion batteries are closely related to the safety of electric vehicles. Accurate peak power and state of charge prediction can extend battery life while ensuring safe driving. In this paper, a modeling strategy for the joint estimation of the battery state of charge and peak power is proposed to consider the effect of current measurement deviation. First, a modified Thevenin model of the battery considering the internal polarization reaction process and the open-circuit voltage hysteresis effect is developed to improve the physical significance of the parameter identification results. On this basis, a current measurement deviation correction strategy based on the double-layer forgetting factor recursive least squares algorithm is proposed. To solve the nonlinearity and noise disturbance problems of the battery system, an Unscented Kalman filter-based multi-parameter constrained adaptive dynamic state observer is developed and used for the joint estimation of the state of charge and peak power. In particular, multiple parameters such as current, voltage, and state of charge are selected for the prediction of the battery peak power. Experimental results for different complex dynamic conditions at different temperatures show the excellent performance of the proposed modeling method in predicting the validity and accuracy verification of the state of charge and peak power. The proposed method provides a viable theoretical basis for the manufacturing technology of advanced battery management systems.

Keywords: Lithium-ion battery; Peak power; State of charge; Adaptive dynamic state observer; Hysteresis characteristic; Current measurement deviation

* Corresponding authors at: School of Information Engineering, Southwest University of Science and Technology, Mianyang 621010, China (SL. Wang).

E-mail addresses: wangshunli@swust.edu.cn (SL. Wang).

1 Introduction

Currently, rechargeable batteries, especially Lithium-ion Batteries (LIBs), are attracting a lot of attention in fields such as Electric Vehicles (EVs) or Aircraft [1]. To ensure the safe, efficient, and durable operation of LIBs under harsh load conditions, an excellent and effective Battery Management System (BMS) is needed. The main task of BMS is to collect battery parameters, and real-time state estimation includes intelligent control and management functions such as State of Charge (SOC), State of Energy (SOE), State of Power (SOP), State of Health (SOH), battery balancing, and on-board fault diagnosis [2]. However, due to the strong time-varying and nonlinear characteristics of LIBs, as well as the influence of random factors such as driving load and working environment, accurate modeling and reliable peak power prediction remain great challenges [3,4].

Peak power is to evaluate the ultimate capacity of charge and discharge power of LIBs under different SOC, temperature, or aging conditions, and optimistically match the relationship between batteries and vehicle dynamic performance to meet the acceleration and climbing performance of EVs (battery discharge power), and maximize the function of click regenerative braking energy recovery (battery charge power) [5]. Peak power prediction has important theoretical significance and application value for the rational use of batteries, avoiding overcharge and over-discharge or overcharge and under voltage of batteries, and prolonging the service life of batteries [6].

Peak power prediction methods mainly include test analysis, data-driven method, and model-based multi-parameter constraint method [7,8]. Test analysis is the most direct method to estimate the peak power by establishing a map of the relevant parameters. This method requires a static test environment and is not applicable in dynamic conditions. The data-driven method is highly accurate, but it has a high dependence on training data and high requirements on the required data processing hardware. The model-based multi-parameter constraint method is combined with the battery model to evaluate the peak power by using filters and other methods, which have the advantages of high reliability and strong robustness of the model

method [9].

The model-based multi-parameter constraint method has an arbitration mechanism, that is, limit constraint conditions. These include cut-off voltage, maximum allowable current, maximum allowable power, SOC, SOE, temperature and life, etc. [10]. Since peak power is calculated based on SOC and temperature, the accuracy of peak power depends on the accuracy of the LIBs temperature acquisition and the accuracy of the SOC.

The peak power of a LIBs is closely related to its temperature because the temperature will affect the rate of the chemical reaction process inside the battery and the characteristics of the battery material, and then affect the current and voltage characteristics of the battery, thus affecting its peak power output [11]. Therefore, the accuracy of battery temperature acquisition is very important for the accuracy of peak power.

On the other hand, the SOC of LIBs also affects its peak power output. SOC management of LIBs requires real-time monitoring and recording of the battery's charge and discharge process to predict and control the battery's peak power output. However, the accuracy of battery SOC is affected by many factors, including SOC estimation methods, model accuracy, and measurement errors [12]. Therefore, to accurately calculate the peak power of the battery, it is necessary to establish an accurate battery model and adopt a high-precision SOC estimation method to obtain more accurate SOC estimation results, and to improve the accuracy of the peak power.

LIB is an electrochemical system with strong time-varying, nonlinear, and distributed parameters, which have many influencing factors and uncertainties, so it is impossible to measure its internal state directly. To estimate the internal state of a power battery accurately, it is necessary to establish a battery model that accurately represents the external characteristics of the battery and is easy to apply in engineering. At present, the Equivalent Circuit Model (ECM) is commonly used as the battery model in the model-based multi-parameter constraint method [13,14]. Among them, the Thevenin model takes into account the accuracy of the ECM and the complexity of calculation, and can effectively characterize the polarization effect of power LIBs [15]. However, due to the characteristics of battery materials, under the same SOC and different charging and discharging conditions, the balance potential of the battery will be different, which is also called the phenomenon of battery hysteresis [16]. Hysteresis is the main

cause of SOC and Open Circuit Voltage (OCV) curve errors. At the same time, the SOC and OCV curves have very complex nonlinearity, and the hysteresis loop in the open circuit voltage curve is easy to cause large errors in the model prediction. Given the influence mechanism of the hysteresis effect on modeling, relevant scholars introduced hysteresis voltage to improve the accuracy of battery modeling [17-19].

To predict the peak power of LIBs, the parameters of the ECM must first be obtained. However, there is a current input to the actual battery that produces an end voltage response to the battery, while the current is also input to the ECM, which also produces a model voltage response. When the model is not accurate, there will be an error between the two terminal voltage responses, which can be used to adjust the state and parameters of the response. Therefore, parameter values must be updated online to achieve the coupling between parameter identification and state estimation, to accurately predict the peak power. At present, the main online parameter identification method commonly used are Recursive Least Squares (RLS) algorithm. The RLS method realizes the identification of real-time parameters through the principle of least mean square error. Because the phenomenon of "Data saturation" occurs after the algorithm of the RLS algorithm has too much data, the error of parameter identification becomes larger. Researchers [20,21] put forward an RLS algorithm based on forgetting factors, which avoids data saturation by adding Forgetting Factors (FF), to improve the accuracy of online parameter identification.

Accurate estimation of the battery SOC as one of the peak power prediction constraints is critical. Common SOC estimation methods include the OCV method, Amp-Hour (AH) integrator method, data-driven method, and model-based method [22]. The OCV method is simple in principle and low in calculation though. However, the method does not meet the real-time requirements and is sensitive to sensor accuracy. The calculation of the AH Integrator method is simple and time-consuming. However, the method also suffers from initial SOC uncertainty and cumulative errors caused by sensor drift. Therefore, it is common to use the AH Integrator method in combination with other methods. Data-driven methods are less sensitive to model accuracy and environmental conditions. The disadvantages of these methods are that they are computationally expensive and computationally time-consuming, and the accuracy of the algorithm is greatly dependent on the training data. Model-based methods,

including filter-based and observer-based methods, have high estimation accuracy and robustness to noise. However, the accuracy of this class of methods usually depends on the accuracy of the model and requires more computational parameters due to the complexity of the algorithm.

At present, the main filter methods commonly used are the Extended Kalman filter (EKF) and the Unscented Kalman filter (UKF) [23,24]. Although the Kalman Filter (KF) provides an effective solution to the linear Gaussian filtering problem, it is difficult to obtain satisfactory filtering results for non-Gaussian distributions. To solve the problem of non-Gaussian noise interference in the EKF algorithm, an adaptive EKF algorithm based on the maximum correlation entropy criterion was proposed in the literature [25] for improving the estimation accuracy of SOC. To address the divergence problem caused by the noise covariance matrix in the UKF algorithm, an Adaptive Fractional-order Square Root Unscented Kalman filter was developed in the literature [26] for updating the noise information in real-time, thus improving the SOC estimation accuracy. For peak battery power prediction, multi-parameter constraint methods are often combined with methods such as battery model-based filters. The literature [27] uses the Adaptive Unscented Kalman filter (AUKF) to establish a joint estimation algorithm for the SOP and SOE and to verify the effectiveness of the algorithm. The literature [28] proposed a fractional-order ECM and estimated SOP with SOC, voltage, and current as constraints, and the validation showed that the multi-parameter constrained approach has high estimation accuracy. The multiple constraints on the peak power co-prediction can effectively form the complementary on the defects of each method, which is of great research significance.

However, in most complex systems, it is not possible to measure the entire state vector directly, when an appropriate approximation of the state vector is required. Unlike the KF, the observer aims to design a dynamic system that can produce an approximation of the state vector, whose properties can be determined to some extent freely by the designer. When the entire state is unavailable, the dynamic system enters the entire design process through its introduction. The state observer can obtain estimates of the state variables based on the measured values of the external variables of the system. The state observer not only offers practical possibilities for the implementation of state feedback techniques but also has applications in many aspects of control engineering. In recent years, the observer-based approach has been used extensively for

battery state estimation. The literature [29] investigates in detail the effect of measurement noise on the identification of the parameters of the first-order RC-ECM, using RLS for the cooperative estimation of the model parameters and the noise variance, and the real-time evaluation of the SOC in combination with the Luenberger observer.

It is worth noting that Current Measurement Deviation (CMD) is a non-negligible issue in the algorithm of the BMS for practical applications. Since the battery current is an important input parameter for ECM parameter identification, the presence of CMD has a significant impact on the battery modeling [30]. Then, the uncalibrated AH Integrator method, it will lead to increasing errors in the SOC estimation. In addition, CMD will affect the inaccuracy of peak battery power prediction as the SOC estimation error increases. For the presence of CMD, the literature [31] proposed a method based on an unbiased ECM to eliminate the current deviation, which effectively attenuates the current deviation. The literature [32] used a drift current corrector, to suppress the effect of drift current. However, the convergence of these two methods is slow and unstable. Therefore, it is necessary to propose a stable and accurate CMD correction method.

In summary, this paper proposes an adaptive dynamic state observer with multi-parameter constraints considering the hysteresis characteristics and CMD correction to predict the SOC and peak power of the LIBs. The details of this policy are shown below.

(1) Considering the dual exponential requirements of computational complexity and model accuracy, a high-fidelity Thevenin model based on the consideration of battery polarization and hysteresis phenomena is established to approximate the high nonlinearity of LIBs and to achieve accurate characterization of the external battery properties.

(2) To reduce the impact of CMD on modeling and state estimation, a CMD correction strategy based on the Double-Layer Forgetting Factor Recursive Least Squares (DLFFRLS) algorithm is proposed to make the identification results of key parameters of the battery model have a clear physical meaning.

(3) To solve the nonlinearity problem of battery system state estimation and suppress noise interference, an adaptive dynamic state observer based on improved UKF is used for joint SOC and peak power prediction.

2 Theoretical Analysis

The BMS has charge and discharge control as one of its main tasks. When the battery is not charged or discharged properly, such as over-charging or over-discharging, it will cause permanent damage to the battery. Therefore, the predicted power capability of the battery based on voltage, current, and SOC constraints is used as an indicator for charge and discharge management. Accurate power prediction not only ensures safety but also regulates driving behavior and optimizes battery energy utilization. The block diagram of SOC and peak power prediction for LIBs in this paper as shown in Figure 1.
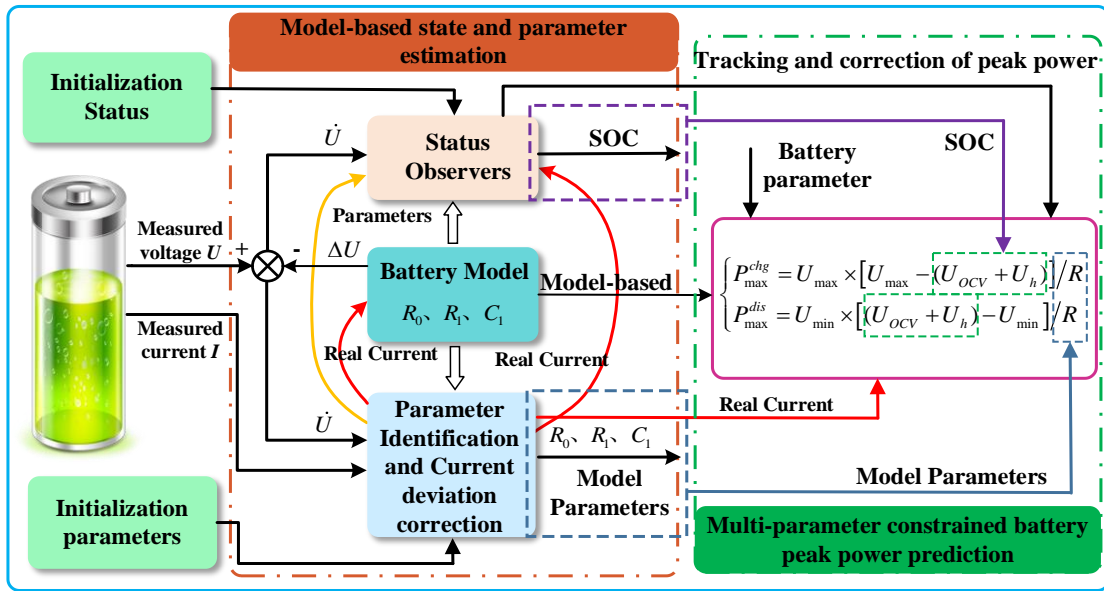

Figure 1 SOC and Peak Power Prediction Framework for LIBs

2.1 Battery model considering hysteresis and polarization phenomena

Since the battery is a strongly time-varying nonlinear system, there are effects of hysteresis characteristics during the charge and discharge process, which cause deviations between the SOC and OCV, thus influencing the estimation of parameters such as the polarization voltage of the battery. For the presence of hysteresis effects, the hysteresis voltage is one of the main factors of the SOC-OCV curve errors caused [33]. Therefore, the hysteresis phenomenon should be considered in the ECM. The ECM of the battery considering the hysteresis and
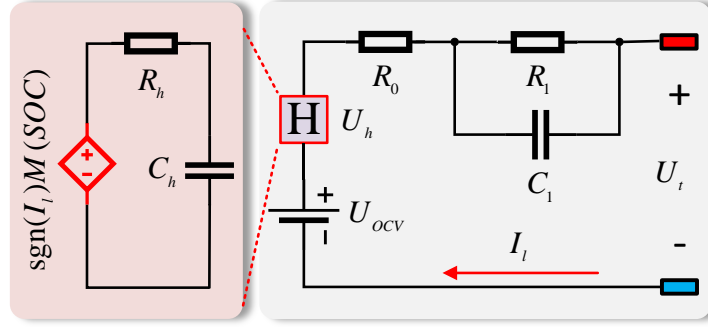
polarization phenomena is shown in Figure 2.

Figure 2 ECM considering hysteresis and polarization phenomena

In Figure 2, the resistance R_0 is the ohmic internal resistance of LIBs. The RC network is used to represent the polarization phenomenon of LIBs. Where, the resistance R_1 is the LIBs polarization internal resistance, and the capacitor C_1 is the LIBs polarization capacitance. The OCV source U_{ocv} is parameterized as a nonlinear function of the battery SOC and is used to describe the equilibrium potential of the LIBs. The hysteresis voltage U_h indicates the hysteresis characteristic. Therefore, the equations of polarization voltage and the terminal voltage of LIBs are shown in equation (1).

$$\begin{cases} U_{1,k} = U_{1,k-1}e^{\frac{-\Delta t}{\tau_1}} - (1-e^{\frac{-\Delta t}{\tau_1}})R_1 I_{l,k} \\ U_{t,k} = U_{ocv,k} - R_0 I_{l,k} - U_{1,k} + U_{h,k} \end{cases} \tag{1}$$

In equation (1), $U_{1,k}$ is the polarization voltage of the LIBs at the kth moment, $U_{t,k}$ is the terminal voltage of the LIBs at the kth moment, $U_{ocv,k}$ is the OCV of the LIBs at the kth moment, $U_{h,k}$ is the LIBs hysteresis voltage at the kth moment and $I_{l,k}$ is the load current at the kth moment. Where $\tau_1 = R_1 C_1$ and $\Delta t = 0.1s$.

For the hysteresis effect present in LIBs, the differential equation describing the ECM hysteresis voltage is shown in equation (2).

$$\frac{dU_h}{dSOC} = -\gamma sign(I_l)U_h + \gamma M(SOC) \tag{2}$$

Where $1/\gamma$ is the charge constant, γ is identified by the undetermined coefficient method, and the identification result is 2.9815×10^{-4}.

$M(SOC)$ represents the hysteresis voltage, and the hysteresis voltage is shown in equation (3).

$$M(SOC) = (U_{ocv,chg} - U_{ocv,dischg})/\xi \qquad (3)$$

Where ξ is the coefficient of the hysteresis voltage and ξ is set to 2.

The hysteresis voltage can then be calculated by equation (4).

$$U_{h,k} = e^{\frac{-\Delta t}{\tau_h}} U_{h,k-1} + (1 - e^{\frac{-\Delta t}{\tau_h}})M[I_l, SOC] \qquad (4)$$

In equation (4), $M[I_l, SOC] = sgn(I_l)M(SOC)$, $\tau_h = R_h C_h$, R_h and C_h are the resistance and capacitance of the battery hysteresis voltage approximation, and C_h =1F is set.

First, assume that the hysteresis voltage approximation characterizes [4] the resistance R_h as shown in equation (5).

$$R_h = \frac{Q_N}{\gamma |I_l|} \qquad (5)$$

Where Q_N is the rated capacity of the battery.

The open circuit voltage U_{ocv} equation is shown in equation (6).

$$U_{ocv} = (U_{ocv,chg} + U_{ocv,dischg})/\rho \qquad (6)$$

In equation (6), $U_{ocv,chg,}$ and $U_{ocv,dischg}$ is the OCV during charge and discharge, and ρ is the OCV factor. In this paper, we analyze the hysteresis characteristics with ρ set to 2. Details are given in the hysteresis characteristics analysis section of Section 3.1.

The polynomial fitting function for the U_{ocv} is shown in equation (7).

$$U_{ocv}(SOC) = p_0 + p_1 SOC + p_2 SOC^2 + p_3 SOC^3$$
$$+ p_4 SOC^4 + p_5 SOC^5 + p_6 SOC^6 \qquad (7)$$

Where $p_0 \sim p_6$ are polynomial coefficients.

2.2. Parameter identification based on CMD correction

Accurate identification of the ECM parameters is the working basis for the accurate prediction of the peak power of LIBs. In response to the "filter saturation" phenomenon in RLS [34] and the impact of CMD on parameter identification, the CMD correction strategy based on the DLFFRLS algorithm is used in this paper to enable the accurate identification of key parameters of the ECM.

It is assumed that the LIBs characteristics are represented as shown in equation (8).

$$E_{t,k} = U_{t,k} - U_{ocv,k} - U_{h,k} \qquad (8)$$

Equation (8) combined with equation (1) then gives:

$$E_{t,k} = -R_0 I_{l,k} + e^{\frac{-\Delta t}{\tau_1}} E_{t,k-1} + [e^{\frac{-\Delta t}{\tau_1}} R_0 - (1-e^{\frac{-\Delta t}{\tau_1}})R_1]I_{l,k-1} \tag{9}$$

The polynomial coefficients of the model parameters are obtained by definition as shown in equation (10).

$$\begin{cases} \alpha_0 = -R_0 \\ \alpha_1 = e^{\frac{-\Delta t}{\tau_1}} \\ \alpha_2 = e^{\frac{-\Delta t}{\tau_1}} R_0 - (1-e^{\frac{-\Delta t}{\tau_1}})R_1 \end{cases} \tag{10}$$

Where $\alpha_0 \sim \alpha_2$ are the parameter coefficients.

Rewrite equation (10) as shown in equation (11).

$$E_{t,k} = \alpha_0 I_{l,k} + \alpha_1 E_{t,k-1} + \alpha_2 I_{l,k-1} \tag{11}$$

Define the parameter output vector and the data input vector as shown in equation (12).

$$\begin{cases} \theta_{LS,k} = \begin{bmatrix} \alpha_{0,k} & \alpha_{1,k} & \alpha_{2,k} \end{bmatrix} \\ \varphi_{LS,k} = \begin{bmatrix} I_{l,k} & E_{t,k-1} & I_{l,k-1} \end{bmatrix} \end{cases} \tag{12}$$

In equation (12), $\theta_{LS,k}$ is the system parameter output vector and $\varphi_{LS,k}$ is the system data input vector, and $y_{LS,k} = \theta_{LS,k}\varphi_{LS,k}^T$.

Among them, the output of the observable system for the parameter identification part is shown in equation (13).

$$y_{LS,k} = \theta_{LS,k}\varphi_{LS,k}^T + e_{LS,k} \tag{13}$$

In equation (13), $y_{LS,k}$ is the system output variable and $e_{LS,k}$ is the smooth zero-mean white noise.

The battery ECM parameter identification equation is shown in equation (14).

$$\begin{cases} R_{0,k} = -\alpha_{0,k} \\ R_{1,k} = \dfrac{\alpha_{0,k}\alpha_{1,k} + \alpha_{2,k}}{\alpha_{1,k} - 1} \\ C_{1,k} = \dfrac{1-\alpha_{1,k}}{(\alpha_{0,k}\alpha_{1,k} + \alpha_{2,k})\log(\alpha_{1,k})} \end{cases} \tag{14}$$

The prediction error based on the FFRLS1 parameter identification is shown in equation (15).

$$e_{LS,k} = E_{t,k} - \theta_{LS,k}\varphi_{LS,k}^T \tag{15}$$

Then the computational flow of FFRLS1 parameter identification is shown in equation (16).

$$\begin{cases} K_{LS,k} = P_{LS,k-1}\varphi_{LS,k}^T \left[\lambda + \varphi_{LS,k}P_{LS,k-1}\varphi_{LS,k}^T \right]^{-1} \\ P_{LS,k} = \dfrac{1}{\lambda}\left[I - K_{LS,k}\varphi_{LS,k}^T \right]P_{LS,k-1} \\ \hat{\theta}_{LS,k} = \hat{\theta}_{LS,k-1} + K_{LS,k}\left[y_{LS,k} - \hat{\theta}_{LS,k-1}\varphi_{LS,k}^T \right] \end{cases} \tag{16}$$

In equation (16), λ is the forgetting factor of the parameter identification part of the first layer FFRLS1, and λ is set to 0.98 in this paper; $K_{LS,k}$ is the gain of the FFRLS1 algorithm; $P_{LS,k}$ is the covariance matrix of the state estimates of the FFRLS1 algorithm, and I is the unit matrix.

In the actual use of BMS, it will be affected by the ambient temperature, sensor accuracy, and other factors, resulting in the phenomenon of CMD. The presence of CMD reduces the accuracy of battery modeling and state estimation. Therefore, it is necessary to correct the CMD.

Suppose the kth sampling point of the measured current obtained directly by the BMS is defined as $I_{m,k}$, which is related to $I_{l,k}$ as shown in equation (17).

$$I_{m,k} = I_{l,k} + I_{b,k} \tag{17}$$

Where $I_{b,k}$ is the CMD value at the kth moment.

Assuming the premise of the current measurement without any deviation, the model parameters are obtained according to the algorithm of the first layer. A second layer of algorithms will be used to correct the CMD. The prediction of the dynamic battery voltage $E_{m,k}$ is calculated using $I_{m,k}$ and $\theta_{m,k}$, and the dynamic battery voltage equation is shown in equation (18).

$$E_{m,k} = \hat{\alpha}_{0,k}I_{m,k} + \hat{\alpha}_{1,k}E_{m,k-1} + \hat{\alpha}_{2,k}I_{m,k-1} \tag{18}$$

In equation (18), $\hat{\alpha}_0$, $\hat{\alpha}_1$ and $\hat{\alpha}_2$ are the matrix elements of the second layer algorithm $\theta_{m,k}$, and $E_{m,k-1}$ is the value of $E_{m,k}$ at the previous moment.

The error calculation equation of $E_{m,k}$ and $E_{t,k}$ is shown in equation (19).

$$\begin{aligned} b_k &= E_{m,k} - E_{t,k} \\ &= \hat{\alpha}_{0,k}I_{m,k} + \hat{\alpha}_{1,k}E_{m,k-1} + \hat{\alpha}_{2,k}I_{m,k-1} - \hat{\alpha}_{0,k}I_{l,k} - \hat{\alpha}_{1,k}E_{t,k-1} - \hat{\alpha}_{2,k}I_{l,k-1} \\ &= \hat{\alpha}_0 I_{b,k} + \hat{\alpha}_1 b_k + \hat{\alpha}_2 I_{b,k-1} \end{aligned} \tag{19}$$

Where b_k is the dynamic voltage error caused by the CMD and $E_{t,k}$ is the predicted dynamic battery voltage. Define the CMD voltage error equation as shown in equation (20).

$$y_{Lb,k} = \theta_{Lb,k}\varphi_{Lb,k}^T \qquad (20)$$

Where $y_{Lb,k} = b_k - \hat{\alpha}_1 b_{k-1}$, $\varphi_{Lb,k} = [\hat{\alpha}_0 \quad \hat{\alpha}_2]^T$, $\theta_{Lb,k} = [I_{b,k} \quad I_{b,k-1}]^T$. In equation (20), $y_{Lb,k}$ is the CMD voltage error system output, $\varphi_{Lb,k}$ is a known data vector, and the parameter vector $\theta_{Lb,k}$ is obtained by the FFRLS2 algorithm. The second layer of the algorithm flow is shown in equation (21).

$$\begin{cases} K_{Lb,k} = P_{Lb,k-1}\varphi_{Lb,k}^T \left[\mu + \varphi_{Lb,k} P_{Lb,k-1}\varphi_{Lb,k}^T \right]^{-1} \\ P_{Lb,k} = \dfrac{1}{\mu}\left[I - K_{Lb,k}\varphi_{Lb,k}^T \right] P_{Lb,k-1} \\ \hat{\theta}_{Lb,k} = \hat{\theta}_{Lb,k-1} + K_{Lb,k}\left[y_{Lb,k} - \hat{\theta}_{Lb,k-1}\varphi_{Lb,k}^T \right] \end{cases} \qquad (21)$$

Where $K_{Lb,k}$ and $P_{Lb,k}$ are the gain and data covariance matrices of the FFRLS2 algorithm; μ is the forgetting factor of the second stage algorithm, and in this paper, μ is set to 0.97.

The CMD correction strategy based on the DLFFRLS algorithm is shown in Figure 3.
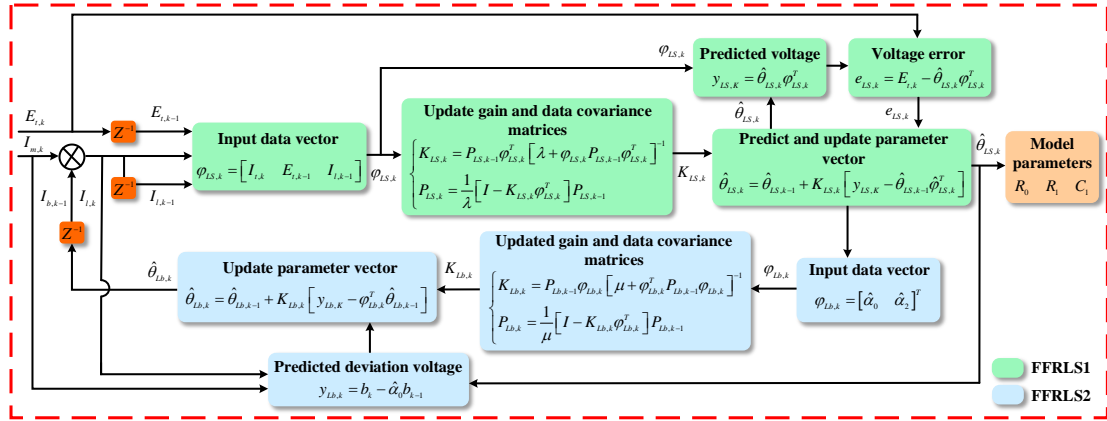

Figure 3. CMD correction strategy based on DLFFRLS algorithm

In Figure 3, the first layer of the FFRLS1 algorithm identifies the ECM parameters. Where $\hat{\alpha}_0$ and $\hat{\alpha}_2$ obtained in the FFRLS1 algorithm is used as input parameters for the second layer of the FFRLS2 algorithm to obtain the CMD and make corrections. In the case that the CMD estimated by the FFRLS2 algorithm is more accurate, the FFRLS1 algorithm can guarantee the accuracy of the battery model parameters.

2.3 Peak power prediction with multi-parameter constraints

The working current of LIBs for EVs is a random variable determined by the road driving conditions, which causes the peak power to vary with the battery working conditions. Assuming

that the battery current is positive when discharging, it is negative when charging. The minimum peak power and maximum peak power for the charge and discharge of LIBs are defined as shown in equation (22).

$$\begin{cases} P_{\min}^{chg} = \max\left(P_{\min}, U_{t,k+L}I_{\min}^{chg}\right) \\ P_{\max}^{dischg} = \min\left(P_{\max}, U_{t,k+L}I_{\max}^{dischg}\right) \end{cases} \tag{22}$$

In equation (22), P_{min}^{chg} is the minimum peak power when charging, and P_{max}^{dischg} is the maximum peak power when discharging. P_{min} is the minimum peak power limit of the battery and P_{max} is the maximum peak power limit of the battery. $U_{t,k+L}$ is the battery terminal voltage at the $k+L$th moment. I_{min}^{chg} is the minimum continuous charging current at the moment k to $k+L$, and I_{max}^{dischg} is the maximum continuous discharging current at the moment k to $k+L$.

Power batteries require both high charging power to absorb braking energy and high discharging power for assisted driving when used in EVs [35]. Therefore, the battery SOC needs to meet the high-power discharge requirements while ensuring that the battery can quickly and efficiently absorb the energy from the feedback.

The LIB SOC is defined as the ratio of the remaining battery capacity to the nominal battery capacity [36]. The equation for calculating the SOC of LIB is shown in equation (23).

$$SOC_{k+1} = SOC_k - \frac{\eta I_{l,k}\Delta t}{Q_N} \tag{23}$$

Where SOC_k is the battery charge state at the kth moment, $I_{l,k}$ is the actual current at the kth moment, η is the capacitance efficiency.

When SOC is used as the constraint parameter, the equation for calculating the continuous charge and discharge current is shown in equation (24).

$$\begin{cases} I_{l,\max}^{dischg,SOC} = \frac{(SOC_k - SOC_{\min})Q_N}{\eta L\Delta t} \\ I_{l,\min}^{chg,SOC} = \frac{(SOC_k - SOC_{\max})Q_N}{\eta L\Delta t} \end{cases} \tag{24}$$

Where $I_{min}^{chg,SOC}$ is the continuous minimum charge current based on SOC constraint, and $I_{max}^{dischg,SOC}$ is the continuous maximum discharge current based on SOC constraint. SOC_{min} is the maximum SOC limit value when discharged, and SOC_{max} is the minimum SOC limit value when charged.

The limiting voltage of LIB is not only a judgment factor for the charge or discharge of the battery, but the limiting voltage is also an analysis of the current output capability of the battery system under the influence of voltage limitation, which is used to determine the power output capability of the battery system. The voltage at the load end at moment $k+L$ can be obtained by equation (1) as shown in equation (25).

$$
\begin{aligned}
U_{t,k+L} &= U_{ocv,k+L} - I_{l,k+L}R_0 - U_{1,k+L} + U_{h,k} \\
&= U_{ocv,k+L} - I_{l,k+L}R_0 - [U_{1,k+L-1}e^{\frac{-\Delta t}{\tau_1}} - (1-e^{\frac{-\Delta t}{\tau_1}})R_1 I_{l,k+L}] + U_{h,k} \\
&= U_{ocv,k+L} - I_{l,k+L}R_0 - [U_{1,k+L-1}e^{\frac{-\Delta t}{\tau_1}} - (1-e^{\frac{-\Delta t}{\tau_1}})\sum_{j=0}^{L-1}(e^{\frac{-\Delta t}{\tau_1}})^{L-1-j} R_1 I_{l,k+L}] + U_{h,k} \\
&= U_{ocv,k+L} - U_{1,k+L-1}e^{\frac{-\Delta t}{\tau_1}} - I_{l,k+L}[R_0 + R_1(1-e^{\frac{-\Delta t}{\tau_1}})\sum_{j=0}^{L-1}(e^{\frac{-\Delta t}{\tau_1}})^{L-1-j}] + U_{h,k}
\end{aligned}
\tag{25}
$$

In equation (25), $U_{t,k+L}$ denotes the load terminal voltage at the $k+L$th moment, $U_{ocv,k+L}$ denotes the open circuit voltage at the $k+L$th moment, $I_{l,k+L}$ denotes the load current at the $k+L$th moment, and $U_{1,k+L}$ denotes the polarization voltage at the $k+L$th moment. Where the OCV at moment $k+L$ is calculated by equation (26).

$$
\begin{aligned}
U_{ocv,k+L} &= f(SOC_{k+L}) \\
&= f(SOC_k - I_{l,k+L}\frac{\eta L\Delta t}{Q_N}) \\
&= U_{ocv,k} - \frac{\partial U_{ocv}}{\partial SOC_k}I_{l,k+L}\frac{\eta L\Delta t}{Q_N}
\end{aligned}
\tag{26}
$$

When the parameters describing the current and voltage are separated, equation (25) can be rewritten as equation (27).

$$
\begin{aligned}
U_{ocv,k+L} = U_{ocv,k} - U_{1,k}e^{\frac{-L\Delta t}{\tau_1}} \\
- I_{l,k+L}\left[\frac{\partial U_{ocv}}{\partial SOC_k}\frac{\eta L\Delta t}{Q_N} + R_0 + R_1\left(1-e^{\frac{-\Delta t}{\tau_1}}\right)\sum_{j=0}^{L-1}\left(e^{\frac{-\Delta t}{\tau_1}}\right)^{L-1-j}\right] + U_{h,k}
\end{aligned}
\tag{27}
$$

With the load terminal voltage as the constraint parameter, the terminal voltage of the battery when charged and discharged is shown in equation (28).

$$
\begin{cases}
0 = U_{ocv,k} - U_{1,k+L-1}e^{\frac{-\Delta t}{\tau_1}} \\
\quad - I_{l,min}^{chg,Volt}[\dfrac{\partial U_{ocv}}{\partial SOC_k}\dfrac{\eta L\Delta t}{Q_N} + R_0 + R_1(1-e^{\frac{-\Delta t}{\tau_1}})\displaystyle\sum_{j=0}^{L-1}(e^{\frac{-\Delta t}{\tau_1}})^{L-1-j}] + U_{h,k} - U_{t,max} \\
0 = U_{ocv,k} - U_{1,k+L-1}e^{\frac{-\Delta t}{\tau_1}} \\
\quad - I_{l,max}^{dischg,Volt}[\dfrac{\partial U_{ocv}}{\partial SOC_k}\dfrac{\eta L\Delta t}{Q_N} + R_0 + R_1(1-e^{\frac{-\Delta t}{\tau_1}})\displaystyle\sum_{j=0}^{L-1}(e^{\frac{-\Delta t}{\tau_1}})^{L-1-j}] + U_{h,k} - U_{t,min}
\end{cases}
\tag{28}
$$

In equation (28), $U_{t,max}$ is the limit voltage when charged, and $U_{t,min}$ is the limit voltage when discharged. $I_{l,min}^{chg,Volt}$ is the continuous minimum charge current based on the end voltage constraint, and $I_{l,max}^{dischg,Volt}$ is the continuous maximum discharge current based on the end voltage constraint.

Therefore, the continuous minimum charge current and maximum discharge current based on voltage constraints are shown in equation (29).

$$
\begin{cases}
I_{l,min}^{chg,Volt} = \dfrac{U_{ocv,k} - U_{1,k+L-1}e^{\frac{-\Delta t}{\tau_1}} + U_{h,k} - U_{t,max}}{\dfrac{\partial U_{ocv}}{\partial SOC_k}\dfrac{\eta L\Delta t}{Q_N} + R_0 + R_1(1-e^{\frac{-\Delta t}{\tau_1}})\displaystyle\sum_{j=0}^{L-1}(e^{\frac{-\Delta t}{\tau_1}})^{L-1-j}} \\[4ex]
I_{l,max}^{dischg,Volt} = \dfrac{U_{ocv,k} - U_{1,k+L-1}e^{\frac{-\Delta t}{\tau_1}} + U_{h,k} - U_{t,min}}{\dfrac{\partial U_{ocv}}{\partial SOC_k}\dfrac{\eta L\Delta t}{Q_N} + R_0 + R_1(1-e^{\frac{-\Delta t}{\tau_1}})\displaystyle\sum_{j=0}^{L-1}(e^{\frac{-\Delta t}{\tau_1}})^{L-1-j}}
\end{cases}
\tag{29}
$$

Based on the terminal voltage constraint parameters, SOC constraint parameters, and the constraint parameters designed by the battery manufacturer, the continuous charge and discharge flow capacity of the peak state under multi-parameter constraints is constructed as shown in equation (30).

$$
\begin{cases}
I_{min}^{chg} = \max\left[I_{l,min}^{chg,SOC}, I_{l,min}^{chg,Volt}, I_{l,min} \right] \\
I_{max}^{dischg} = \min\left[I_{l,max}^{dischg,SOC}, I_{l,max}^{dischg,Volt}, I_{l,max} \right]
\end{cases}
\tag{30}
$$

In equation (30), $I_{l,min}$ is the charge current limit designed by the battery manufacturer and $I_{l,max}$ is the discharge current limit designed by the battery manufacturer.

The resultant equation to calculate the multi-parameter constrained peak power in continuous time is shown in equation (31).

$$
\begin{cases}
P_{\min}^{chg} = \max\{P_{\min}, U_{t,k+L} \max(I_{l,\min}^{chg,SOC}, I_{l,\min}^{chg,Volt}, I_{l,\min})\} \\
P_{\max}^{dischg} = \min\{P_{\max}, U_{t,k+L} \min(I_{l,\max}^{dischg,SOC}, I_{l,\max}^{dischg,Volt}, I_{l,\max})\}
\end{cases}
\tag{31}
$$

2.4 Adaptive Dynamic State Observer

The state parameters of LIBs visually reflect the battery performance, and accurate state estimation helps in the construction of the battery energy consumption strategy and the control of the battery system. The state space equations of the battery SOC and polarization voltage are obtained after discretization from equation (1) as shown in equation (32).

$$
\begin{cases}
\begin{bmatrix} U_{1,k} \\ U_{h,k} \\ SOC_k \end{bmatrix} =
\begin{bmatrix}
e^{\frac{-\Delta t}{\tau_1}} & & \\
& e^{\frac{-\Delta t}{\tau_h}} & \\
& & 1
\end{bmatrix}
\begin{bmatrix} U_{1,k-1} \\ U_{h,k-1} \\ SOC_{k-1} \end{bmatrix} \\
\qquad +
\begin{bmatrix}
(1-e^{\frac{-\Delta t}{\tau_1}})R_1 & \\
& 1-e^{\frac{-\Delta t}{\tau_h}} \\
\dfrac{-\eta\Delta t}{Q_N} &
\end{bmatrix}
\begin{bmatrix} I_{l,k-1} \\ M(SOC,I_l) \end{bmatrix} + w_k \\
U_{t,k} = \begin{bmatrix} -1 & 1 & \dfrac{\partial U_{ocv}}{\partial SOC} \end{bmatrix}
\begin{bmatrix} U_{1,k} \\ U_{h,k} \\ SOC_k \end{bmatrix} - R_0 I_{l,k} + v_k
\end{cases}
\tag{32}
$$

Let $x_k = [U_{1,k} \quad U_{h,k} \quad SOC_k]^T$, $y_k = U_{t,k}$, $u_k = [I_{l,k-1} \quad M(SOC,I_l)]^T$. The discrete time-state space equation is abbreviated as shown in equation (33).

$$
\begin{cases}
x_k = f(x_{k-1}, u_k) + w_k \\
y_k = g(x_k, u_k) + v_k
\end{cases}
\tag{33}
$$

Where x_k represents the state vector of the system, y_k represents the observed variables of the system, u_k represents the input variables of the system, w_k represents the process noise of the system, v_k represents the measurement noise of the system, and k represents each moment.

The EKF is one of the algorithms to solve nonlinear filtering, and it is widely used in state estimation. However, the EKF linearizes the battery ECM by Taylor series expansion, ignoring the effect of second-order and higher-order terms, which inevitably introduces linearization

errors [37]. The UKF approximates the mean and variance to the true value step by step through the Unscented transformation (UT) without linearizing the nonlinear system [38]. The UKF is closer to the distribution of state random variables and is more conducive to generating approximate maximum likelihood estimates. Compared with EKF, UKF has higher estimation accuracy and can effectively reduce the error caused by EKF linearization.

However, the process noise and measurement noise of the system need to be set in advance when UKF estimates the state. In practice the state of the battery varies with the operating conditions of the EVs and the uncertainty of the noise leads to an increase in the error of the state prediction [39]. For this reason, this paper uses UKF as a state observer to predict the battery polarization voltage and state. Meanwhile, adaptive factors are introduced to correct the covariance matrices Q_k and R_k in real time to improve the estimation accuracy of SOC and the tracking ability of peak power.

In UKF, the UT is used to calculate the statistics of Gaussian Random Variables (GRV). Nonlinear transformations of Gaussian random variables GRV, whose approximate probability distributions are simpler than approximating arbitrary nonlinear functions. Suppose the mean value of GRV x is $\hat{x}$, UT can generate $2n_a+1$ sigma vectors x points to analyze the data analysis properties of the nonlinear system and select the corresponding weights, as shown in equation (34).

$$
\begin{cases}
\hat{x}_0^a = x_0 \\
\hat{x}_k^a = \hat{x}_k^a + \sqrt{(n_a + \lambda_u) P_k^a}, k = 1 \sim n_a \\
\hat{x}_k^a = \hat{x}_k^a - \sqrt{(n_a + \lambda_u) P_k^a}, k = n_a + 1 \sim 2n_a
\end{cases}
\tag{34}
$$

Where n_a represents the number of state dimensions corresponding to the nonlinear system matrix and P is the system covariance matrix. The described sigma points are weighted to obtain the ability of their distribution points to influence the system, as shown in equation (35).

$$
\begin{cases}
w_0^{(m)} = \dfrac{\lambda_u}{n_a + \lambda_u} \\
w_0^{(c)} = \dfrac{\lambda_u}{n_a + \lambda_u} + 1 - \alpha^2 + \beta \\
w_k^{(m)} = \dfrac{1}{2(n_a + \lambda_u)}, k = 1 \sim 2n_a
\end{cases}
\tag{35}
$$

In equation (35), $\lambda_u = \alpha^2(n_a + \kappa) - n_a$ and λ_u is the sigma scaling parameter; α is the extent to which the sigma point is offset from the state quantity, taking values in the range $1 \times 10^{-4} \le \alpha \le 1$; κ is the auxiliary scaling parameter of the sigma point, usually taken as 0 or $3 - n_a$; β is a non-negative weight coefficient, and β is usually set to 2 when the sigma points become Gaussian distributed; $w^{(m)}$ is the mean weight and $w^{(c)}$ is the covariance weight.

The description of the UKF-based adaptive dynamic state observer is shown below:

Step 1: Initialize the mean and covariance of the system state variables.

$$\begin{cases} \hat{x}_0 = E[x_0] \\ \hat{x}_0^a = E[x^a] \\ P_0 = E[(x_0 - \hat{x}_0)(x_0 - \hat{x}_0)^T] \end{cases} \tag{36}$$

$$P_0^a = E[(x_0^a - \hat{x}_0^a)(x_0^a - \hat{x}_0^a)^T] \tag{37}$$

Step 2: Battery Status Prediction.

(1) Calculate the sigma points.

$$x_{k-1}^a = \left[x_{k-1}^a \quad x_{k-1}^a \pm \sqrt{(n_a + \lambda_u)P_k^a} \right] \tag{38}$$

(2) Status variable time update.

Each sigma point is passed through the state function and the predicted values of the mean and covariance of the state variables at moment k are calculated.

$$x_{k-1}^a = f(x_{k-1}^a, u_k) \tag{39}$$

$$\hat{x}_k^a = \sum_{k=0}^{2n_a} w_k^{(m)} x_k^a \tag{40}$$

$$P_k = \sum_{k=0}^{2n_a} w_k^{(c)} (x_k^a - \hat{x}_k^a)(x_k^a - \hat{x}_k^a)^T + Q_k \tag{41}$$

(3) Measurement variable time update.

Each Sigma point is also passed through the measurement function to calculate the predicted value of the observed variable at moment k.

$$y_k = g(x_k^a, u_k) \tag{42}$$

$$\hat{y}_k = \sum_{k=0}^{2n} w_k^{(m)} y_k \tag{43}$$

(4) Calculate the gain matrix of UKF.

$$K_k = P_{xy,k} P_{y,k}^{-1} \tag{44}$$

$$\begin{cases} P_{y,k} = \sum_{k=0}^{2n_a} w_k^{(c)} (y_k - \hat{y}_k)(y_k - \hat{y}_k)^T \\ P_{xy,k} = \sum_{k=0}^{2n_a} w_k^{(c)} (x_k^a - \hat{x}_k^a)(y_k - \hat{y}_k)^T \end{cases} \tag{45}$$

(5) Noise covariance matrix update.

$$\begin{cases} Q_k = Q_{k-1} + d_{k-1}(K_k \varepsilon_k \varepsilon_k^T K_k^T + P_k - P_{k-1}) \\ R_k = R_{k-1} + d_{k-1}(\varepsilon_k \varepsilon_k^T - P_{y,k}) \\ d_k = (1-b)(1-b^{k+1})^{-1} \\ \varepsilon_k = y_k - \hat{y}_{k-1} \end{cases} \tag{46}$$

Where d_k is the weighting factor, ε_k is the residual of the observed variable, and b is the forgetting factor, which usually takes values in the range of 0.95 ~ 0.99.

(6) Predicted values of state variables and covariance matrix update.

$$\begin{bmatrix} \hat{U}_{1,k} \\ \hat{U}_{h,k} \\ SOC_k \end{bmatrix} = \hat{x}_k = \hat{x}_k^a + K_k(y_k - U_{t,k}) \tag{47}$$

$$P_k = P_{k-1} - K_k P_{y,k} K_k^T \tag{48}$$

Once the state variable prediction is updated, the SOC prediction is obtained.

Step 3: Peak battery power prediction tracks.

(1) Calculation of continuous charge and discharge current based on SOC parameter constraints.

$$\begin{cases} I_{l,max}^{dischg,SOC} = \dfrac{(SOC_k - SOC_{min})Q_N}{\eta L \Delta t} \\ I_{l,min}^{chg,SOC} = \dfrac{(SOC_k - SOC_{max})Q_N}{\eta L \Delta t} \end{cases} \tag{49}$$

(2) Calculation of continuous charge and discharge current based on terminal voltage parameter constraints.

$$\begin{cases} I_{l,\min}^{chg,Volt} = \dfrac{U_{ocv,k} - U_{1,k+L-1}e^{\frac{-\Delta t}{\tau_1}} + U_{h,k} - U_{t,\max}}{\dfrac{\partial U_{ocv}}{\partial SOC_k}\dfrac{\eta L\Delta t}{Q_N} + R_0 + R_1(1-e^{\frac{-\Delta t}{\tau_1}})\sum\limits_{j=0}^{L-1}(e^{\frac{-\Delta t}{\tau_1}})^{L-1-j}} \\[6mm] I_{l,\max}^{dischg,Volt} = \dfrac{U_{ocv,k} - U_{1,k+L-1}e^{\frac{-\Delta t}{\tau_1}} + U_{h,k} - U_{t,\min}}{\dfrac{\partial U_{ocv}}{\partial SOC_k}\dfrac{\eta L\Delta t}{Q_N} + R_0 + R_1(1-e^{\frac{-\Delta t}{\tau_1}})\sum\limits_{j=0}^{L-1}(e^{\frac{-\Delta t}{\tau_1}})^{L-1-j}} \end{cases} \tag{50}$$

(3) Calculation of peak battery power capacity.

$$\begin{cases} P_{\min}^{chg} = \max\{P_{\min},(U_{OCV,k+L} - U_{1,k}e^{\frac{-L\Delta t}{\tau_1}} + U_{h,k} \\ \qquad - \max(I_{l,\min}^{chg,SOC},I_{l,\min}^{chg,Volt},I_{l,\min})(R_0 \\ \qquad + R_1(1-e^{\frac{-\Delta t}{\tau_1}})\sum\limits_{j=0}^{L-1}(e^{\frac{-\Delta t}{\tau_1}})^{L-1-j})\max(I_{l,\min}^{chg,SOC},I_{l,\min}^{chg,Volt},I_{l,\min})\} \\[4mm] P_{\max}^{dischg} = \max\{P_{\max},(U_{OCV,k+L} - U_{1,k}e^{\frac{-L\Delta t}{\tau_1}} + U_{h,k} \\ \qquad - \min(I_{l,\max}^{dischg,SOC},I_{l,\max}^{dischg,Volt},I_{l,\min})(R_0 \\ \qquad + R_1(1-e^{\frac{-L\Delta t}{\tau_1}})\sum\limits_{j=0}^{L-1}(e^{\frac{-L\Delta t}{\tau_1}})^{L-1-j})\min(I_{l,\max}^{dischg,SOC},I_{l,\max}^{dischg,volt},I_{l,\min})\} \end{cases} \tag{51}$$

The strategy of multi-parameter constraints dynamic adaptive observer to predict the SOC and peak power of LIBs considering hysteresis characteristics and CMD correction is shown in Figure 4.
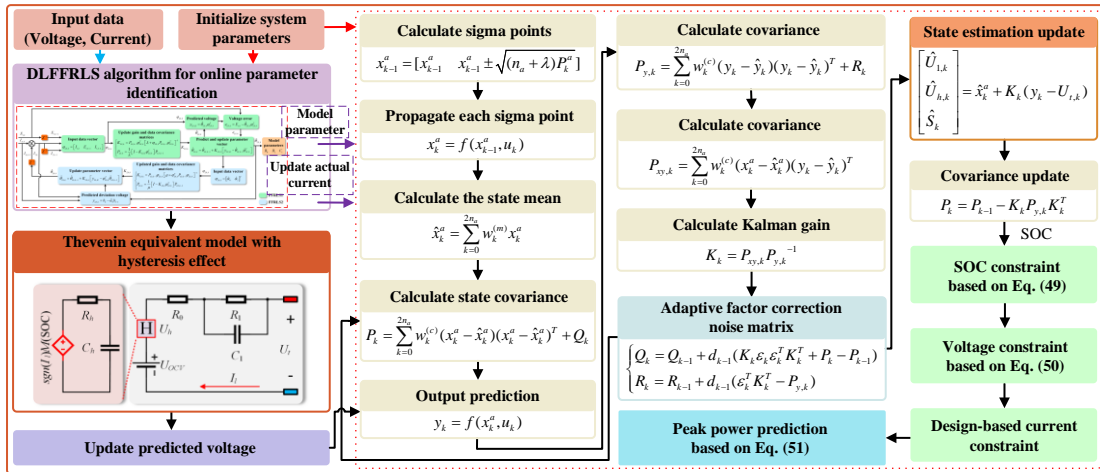

Figure 4. Strategy for prediction of LIB SOC and peak power by a multi-parameter constraint dynamic adaptive observer considering hysteresis characteristics and CMD correction

Through the above analysis, Mean Absolute Error (MAE) and Root Mean Square Error (RMSE) are introduced to evaluate the performance of the algorithm. The MAE and RMSE are

calculated as shown in Equation (52).

$$\begin{cases} MAE = \dfrac{1}{N}\sum\limits_{i=1}^{N}\left|f_i - g_i\right| \\ RMSE = \sqrt{\dfrac{1}{N}\sum\limits_{i=1}^{N}\left(f_i - g_i\right)^2} \end{cases} \qquad (52)$$

MAE and RMSE are visual expressions describing the relationship between the simulated values of the algorithm and the real measured values. In Equation (52), N represents the number of analyses corresponding to the length of observation time for the evaluation strategy. f_i represents the predicted value obtained by the evaluation strategy. g_i represents the true value of the parameter or state obtained through actual testing.

3 Experimental validation and analysis

3.1 Battery charge and discharge test

To verify the feasibility and accuracy of the proposed method, an experimental platform is established for the hysteresis characteristics and working conditions testing of LIBs. The experimental platform is mainly composed of a PC host, battery charge and discharge equipment, and high and low-temperature experimental equipment. The battery experimental platform is shown in Figure 5.
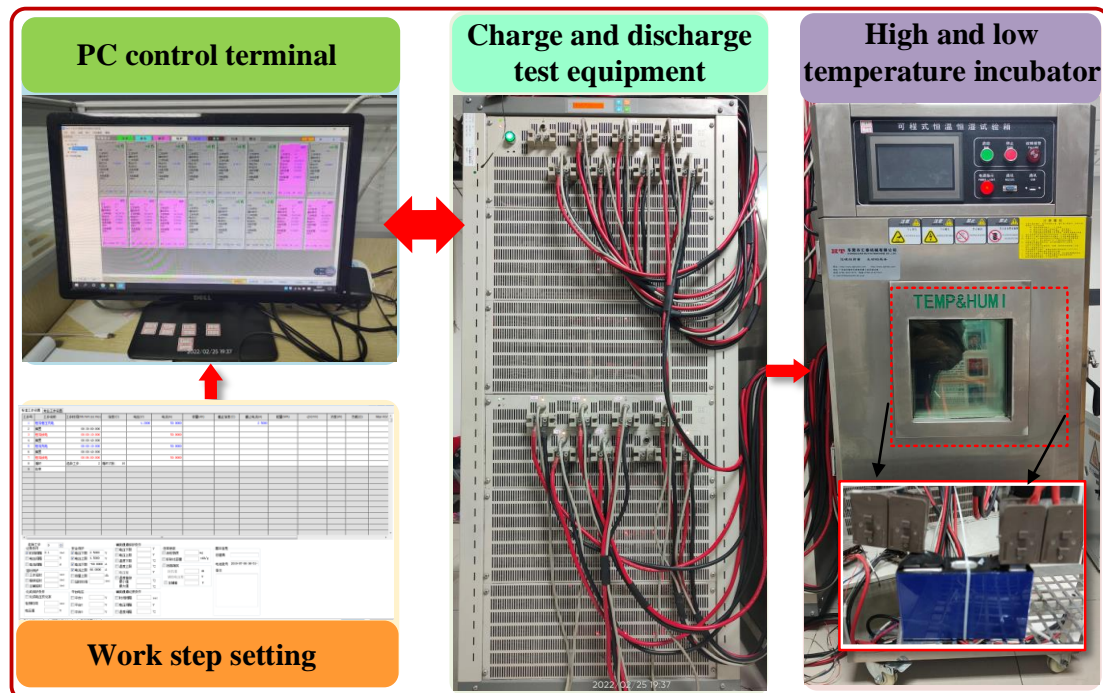
Figure 5. Battery experimental platform

Ternary LIBs are widely used in various fields because of their high energy density and good low-temperature characteristics. Therefore, this paper uses 72Ah automotive ternary LIB to carry out the research. The parameter information of the ternary LIB is shown in Table 1.

Table 1: Parameter information of ternary lithium-ion batteries

Items	Parameters
Battery Capacity	72Ah
Standard Voltage	3.7V
Cut-off volage	4.2V/2.75V
Continuous discharge	3C
Instantaneous discharge	5C
Internal resistance	$\approx 0.5m\Omega$

In this paper, we design a charge and discharge test for the hysteresis effect to deeply investigate the influence of the hysteresis characteristics of LIBs on battery modeling and state estimation. The Beijing Bus Dynamic Stress Test (BBDST) and Dynamic Stress Test (DST) conditions were simulated by the experimental testbed to verify the applicability of the algorithm. The results of the LIB hysteresis characteristics test are shown in Figure 6.
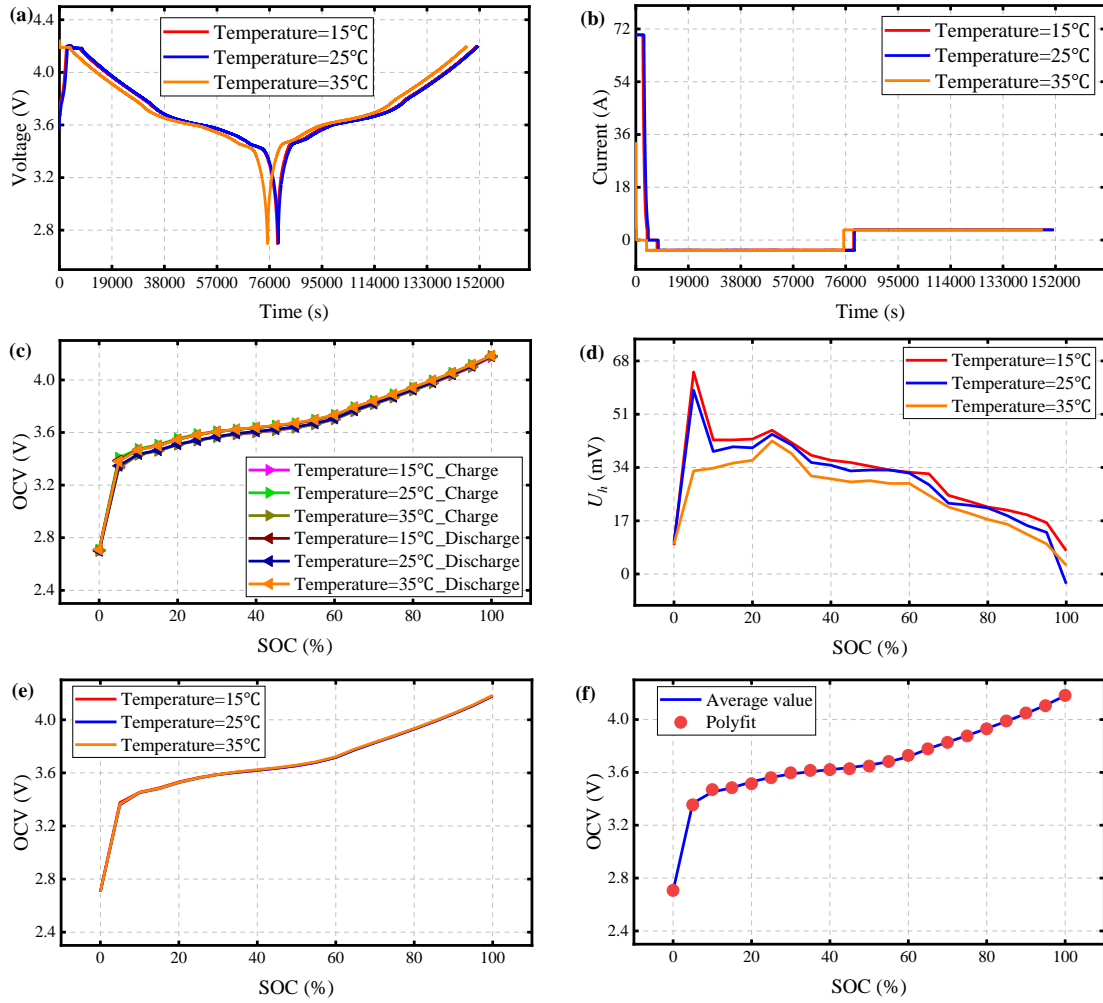
Figure 6. Hysteresis characteristics tests: (a) charge and discharge test voltages at different temperatures; (b) charge and discharge test currents at different temperatures; (c) charge and discharge OCV at different temperatures; (d) hysteresis voltages at different temperatures; (e) average OCV at different temperatures; (f) fitting accuracy of average OCV;

In Figure 6, Figures (a) and (b) show the charge and discharge test voltages and currents designed for the hysteresis effect in this paper, and extract the OCV for charge and discharge at different temperatures. From Figures 6(c) and 6(d), it can be analyzed that when the SOC is low, the hysteresis voltage is affected by the temperature effect more obviously at this time due to the unstable state of the internal material properties of the battery and the further influence of temperature on the battery material. However, as the SOC increases, the internal state of the battery gradually stabilizes and the hysteresis voltage of the charge and discharge OCV gradually decreases. In addition, when the electrode material of the battery is expanded by heat at high temperatures, the diffusion rate of Li+ is accelerated, resulting in a lower concentration

polarization effect of the battery, and the charging and discharging characteristics of the battery are more stable at this time. At low temperatures, the battery material shrinks, the diffusion rate of Li+ slows down, the concentration polarization effect of the battery increases, and the charge and discharge performance of the battery decreases. Therefore, the higher the temperature, the lower the hysteresis voltage, and the less impact it has on the battery modeling and state estimation.

By the above analysis, the hysteresis characteristics and temperature have a certain dependence. To reduce the effect of temperature on the hysteresis characteristics, the OCV at different temperatures is treated by averaging twice in this paper. Among them, Figure 6(e) shows the average values of charge and discharge OCV at 15°C, 25°C, and 35°C. From Figure 6(e), it can be analyzed that the difference between the primary average OCV of the three is small and the temperature has a certain influence on the primary average OCV. To ignore the effect of temperature on OCV, the primary average OCV values at different temperatures are averaged again in this paper. The OCV obtained by two averages is shown in Figure 6(f), and a 6th-order polynomial fit is taken to the OCV of the two averages. In addition, the average values of different temperatures are used in this paper for the hysteresis voltage.

3.2 Verification and analysis of parameter identification based on CMD correction

The accuracy of the parameter identification results of the battery model is measured by the prediction error between the model voltage and the measured voltage. If a CMD exists in the BMS, it is corrected by the DLFFRLS algorithm, while parameter identification is performed. The battery was tested using the BBDST operating conditions at 25°C and the CMD was set artificially by -0.1A. Set the initial values of the DLFFRLS algorithm parameter vector and data vector to: $\hat{\theta}_{LS,0} = [0.1 \quad 0.1 \quad 0.1]^T$, $P_{LS,0} = 10^7 \times diag[0.1 \quad 0.1 \quad 0.1]$, $\hat{\theta}_{Lb,0} = [0.1 \quad 0.1]^T$, $P_{Lb,0} = 10^7 \times diag[0.1 \quad 0.1]$. The results of the ECM parameter identification are shown in Figure 7.
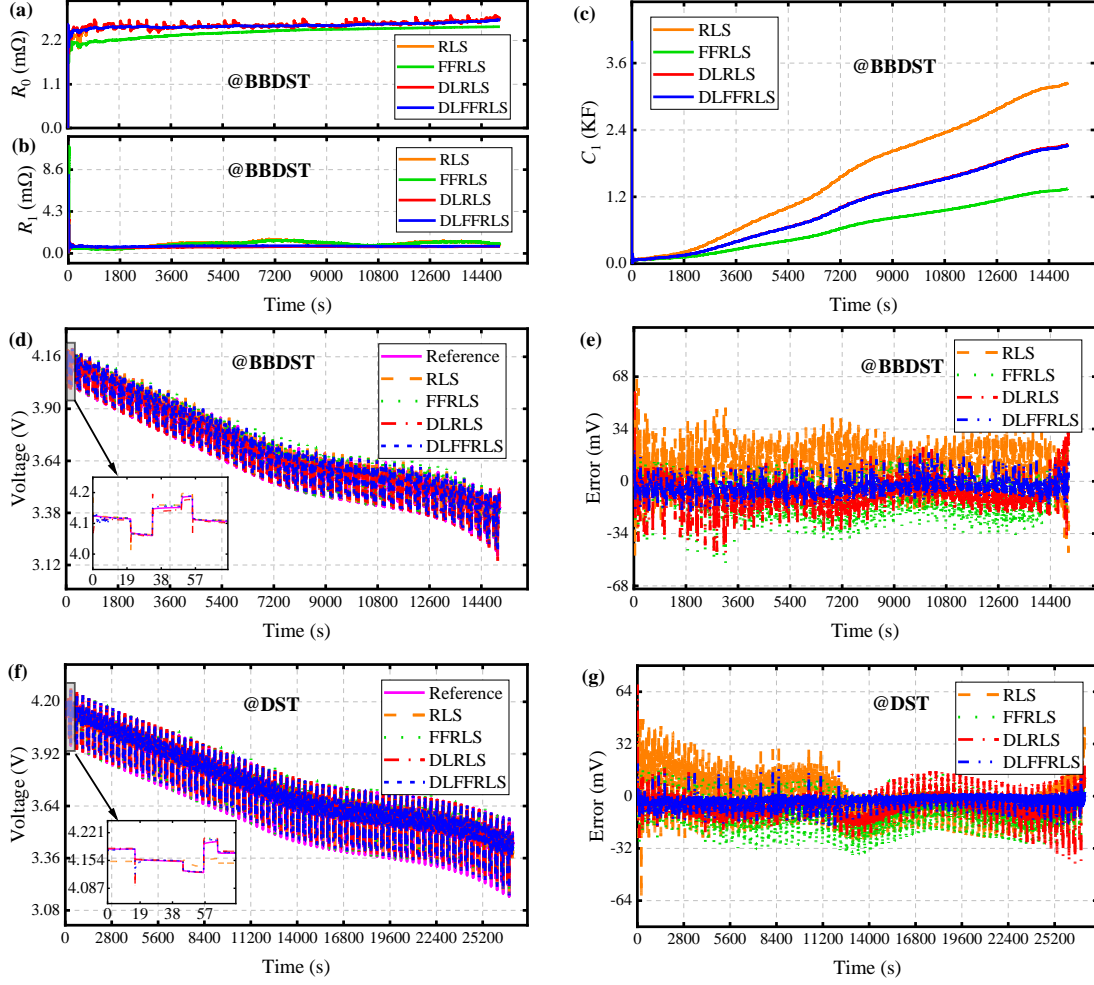
Figure 7. ECM parameter identification results and verification: (a) Identification results of ohmic internal resistance R_0 in BBDST operation; (b) Identification results of polarization resistor R_1 in BBDST operation; (c) Identification results of polarization capacitor C_1 in BBDST operation; (d) Terminal voltage comparison in BBDST operation; (e) Terminal voltage error in BBDST operation; (f) Terminal voltage comparison in DST operation; (g) Terminal voltage error in DST operation;

Figure 7 shows the results of the DLFFRLS algorithm model parameter identification. Since $R_0 \approx \Delta U_1 / \Delta I_1$, the CMD interferes less with the discrimination result of R_0 and the effect of CMD can be almost ignored. Figures 7(d)-(g) depict the estimated results between the model terminal voltage and the measured voltage for BBDST and DST conditions. The errors between the predicted and actual terminal voltages of the RLS and FFRLS algorithms are significantly larger under the interference of CMD. In contrast, the end voltages identified by the DLFFRLS algorithm are closer to the reference end voltages, indicating the good performance of the DLFFRLS algorithm even in the presence of CMD interference.

Table 2 shows the comparison of the end voltage accuracy of different algorithms. In the

presence of CMD interference, under BBDST operating conditions, the RLS algorithm estimates a Root Mean Square Error (RMSE) of 17.32 mV, indicating that this is a poor estimate. The RMSE estimated by the FFRLS algorithm is 14.84 mV, which is an improvement of 2.48 mV for the RLS algorithm discrimination accuracy. While the RMSE of voltage error in the DLRLS algorithm is only 7.93 mV. On the contrary, the RMSE of voltage error in the DLFFRLS algorithm is 4.76 mV and the RMSE of the conventional RLS algorithm is improved by 12.56 mV with high accuracy.

Table 2. Comparison of the terminal voltage accuracy of different algorithms

	BBDST			DST		
	RMSE	MAE	MAX	RMSE	MAE	MAX
RLS	17.32	16.56	67.39	18.37	17.89	68.35
FFRLS	14.84	13.37	48.52	17.52	15.66	47.42
DLRLS	7.93	8.45	60.97	10.18	7.67	20.05
DLFFRLS	4.76	4.19	20.51	5.23	4.55	18.36

From the above analysis, it is concluded that the DLFFRLS algorithm is effective and accurate. The validation results under BBDST and DST conditions show that the DLFFRLS algorithm can accurately identify model parameters and correct CMD with adaptability to different complex operating conditions. Accurate model parameters can reduce system noise and improve the accuracy of SOC estimation, thus improving the prediction of peak battery power.

3.3 Validation and Analysis of SOC Estimation Based on Adaptive Dynamic State Observer

Accurate estimation of battery SOC is necessary as one of the limiting parameters for predicting peak power. The battery environmental temperature is one of the factors that affect the accuracy of SOC estimation. There are significant differences in the charge and discharge characteristics of batteries in different temperature environments. For the effect of temperature environment, BBDST and DST working conditions at temperatures of 15°C, 25°C, and 35°C are used in this paper to verify the accuracy and applicability of the DLFFRLS-AUKF algorithm at different temperatures.

To demonstrate the accurate performance of the DLFFRLS-AUKF algorithm, the UKF, AUKF, RLS-AUKF, and FFRLS-AUKF algorithms are used as comparisons in this paper. The initial value of SOC is set to 0.8, and the initial value of system covariance matrix P_0 is set to $1 \times 10^{-4} \times diag[1 \quad 1 \quad 1]$, the initial value of system process noise covariance Q is set to $8 \times 10^{-11} \times diag[1 \quad 1 \quad 1]$, and the initial value of system measurement noise covariance R is set to 0.05.
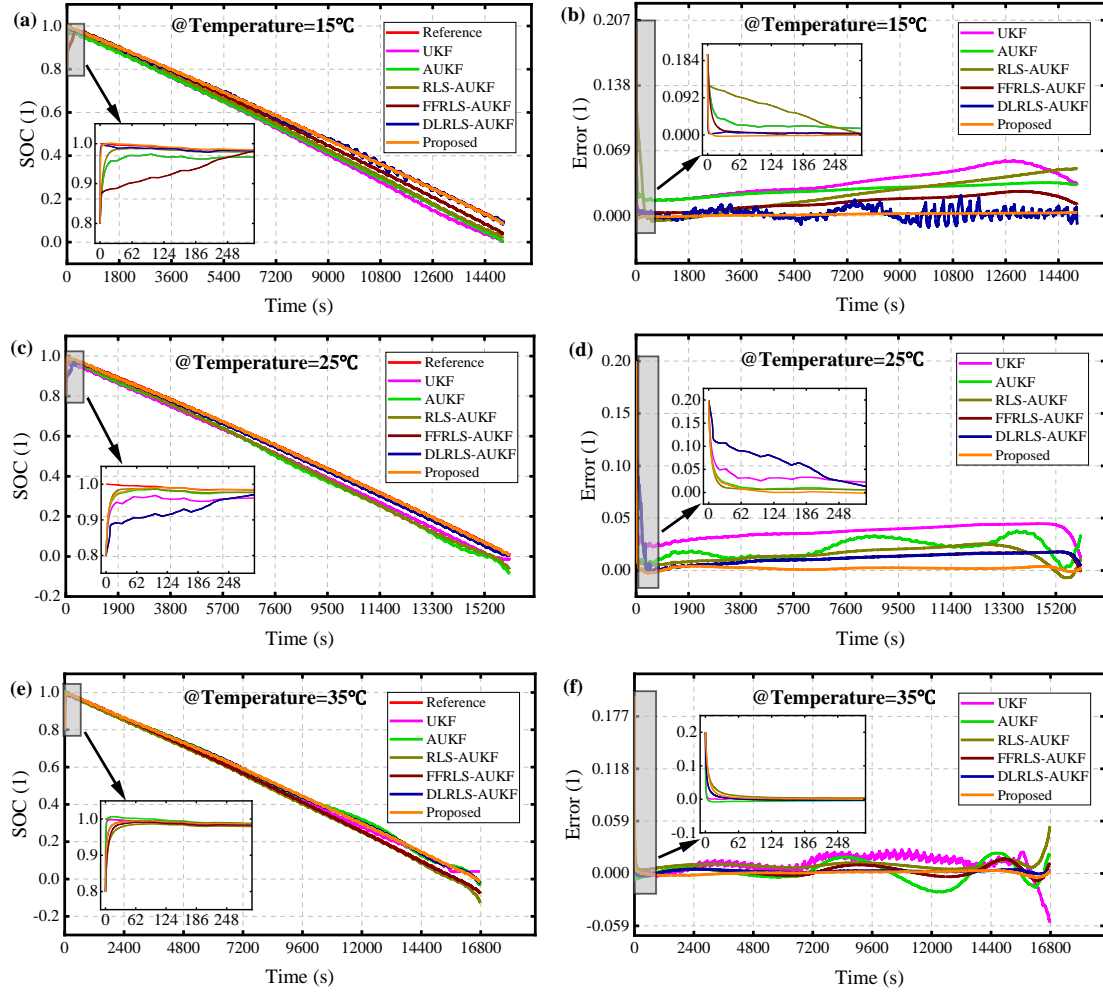
Figure 8. SOC estimation results for BBDST conditions with an initial value of 0.8: (a) 15°C battery SOC estimation result; (b) 15°C battery SOC estimation error; (c) 25°C battery SOC estimation result; (d) 25°C battery SOC estimation error; (e) 35°C battery SOC estimation result; (f) 35°C battery SOC estimation error;
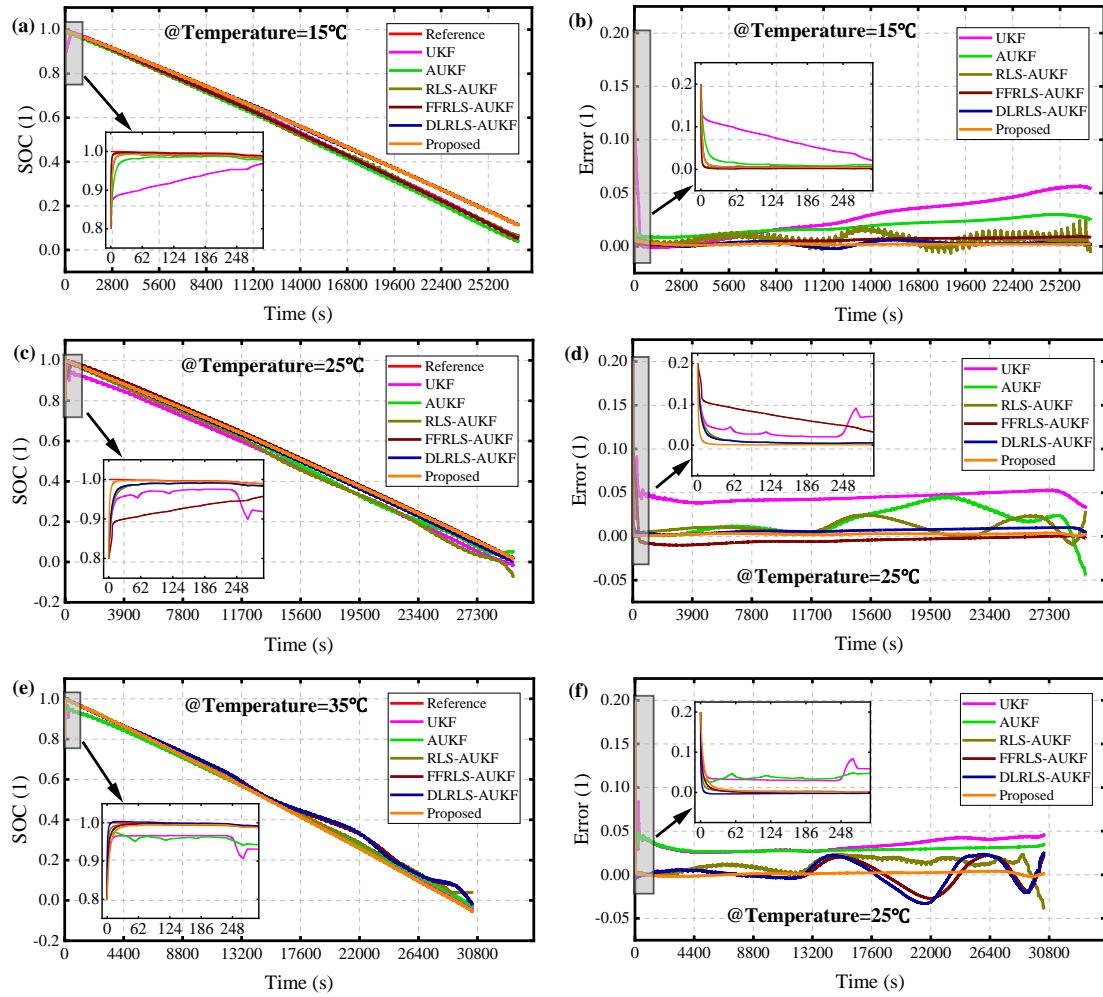
Figure 9. SOC estimation results for DST conditions with an initial value of 0.8: (a) 15°C battery SOC estimation result; (b) 15°C battery SOC estimation error; (c) 25°C battery SOC estimation result; (d) 25°C battery SOC estimation error; (e) 35°C battery SOC estimation result; (f) 35°C battery SOC estimation error;

Figures 8 and 9 show the results of battery SOC estimation for different temperatures for BBDST and DST operating conditions. The proposed algorithm converges rapidly for different temperatures or different operating conditions and can track the trajectory of the reference SOC stably and accurately for an initial error correction of 0.2 for SOC. It is worth noting that the effect of temperature on SOC estimation is more pronounced. For instance, when the temperature is low, the algorithm without temperature correction will gradually diverge, leading to increasing errors.

From Figures 8 and 9, it can be obtained that the estimation error of the proposed method is significantly smaller, with RMSE and MAE less than 0.2%. The convergence times of SOC estimation under BBDST and DST are 7.1s and 10.5s, respectively. The results show that the

method converges quickly and accurately under both BBDST and DST complex conditions.

3.4 Peak Power Prediction Verification and Analysis Based on Adaptive Dynamic State Observer

To verify the performance of the proposed adaptive dynamic state observer, 10s and 50s continuous charge and discharge times are designed in this paper to predict the sustained discharge and charge capability of the algorithm. To avoid overcharge and over-discharge, the SOC constraint for charging and discharging is set to 20% in this paper.

Figure 10 and Figure 11 show the predicted peak power capacity for continuous discharge and charge under BBDST and DST conditions, respectively. Where the continuous discharge and charge are L=10s and L=50s, respectively. In the SOC range from 100% to 0% for complex dynamic conditions, the remaining battery capacity and energy can be almost equal to the maximum available capacity and energy for the charge peak power capability, so the minimum charge current depends mainly on the SOC constraint, which can prevent the battery from being overcharged. The predicted current and power based on SOC parameter constraints are very high and do not allow discharge or charge. Therefore, the voltage parameter constraint is mainly used to predict the minimum charge current during this period.

At the end of battery discharge, the discharge power capability is zero. This is due to the SOC constraint consideration. Therefore, zero-point correction should be added when the SOC range exceeds the SOC limits. Discharge peak power has a decreasing process, but for the 10s peak power is not obvious, the maximum power of the 50s obviously to a decreasing trend. There is a not-so-subtle upward trend in peak charging power, which is due to the small variation interval of SOC, theoretically leading to not much variation in maximum charging power. The predicted peak power errors are small and all within a reasonable range in terms of charging and discharging peak power prediction errors. It is further demonstrated that the proposed multi-parameter constrained dynamic state observer has an accurate prediction effect and strong tracking capability.
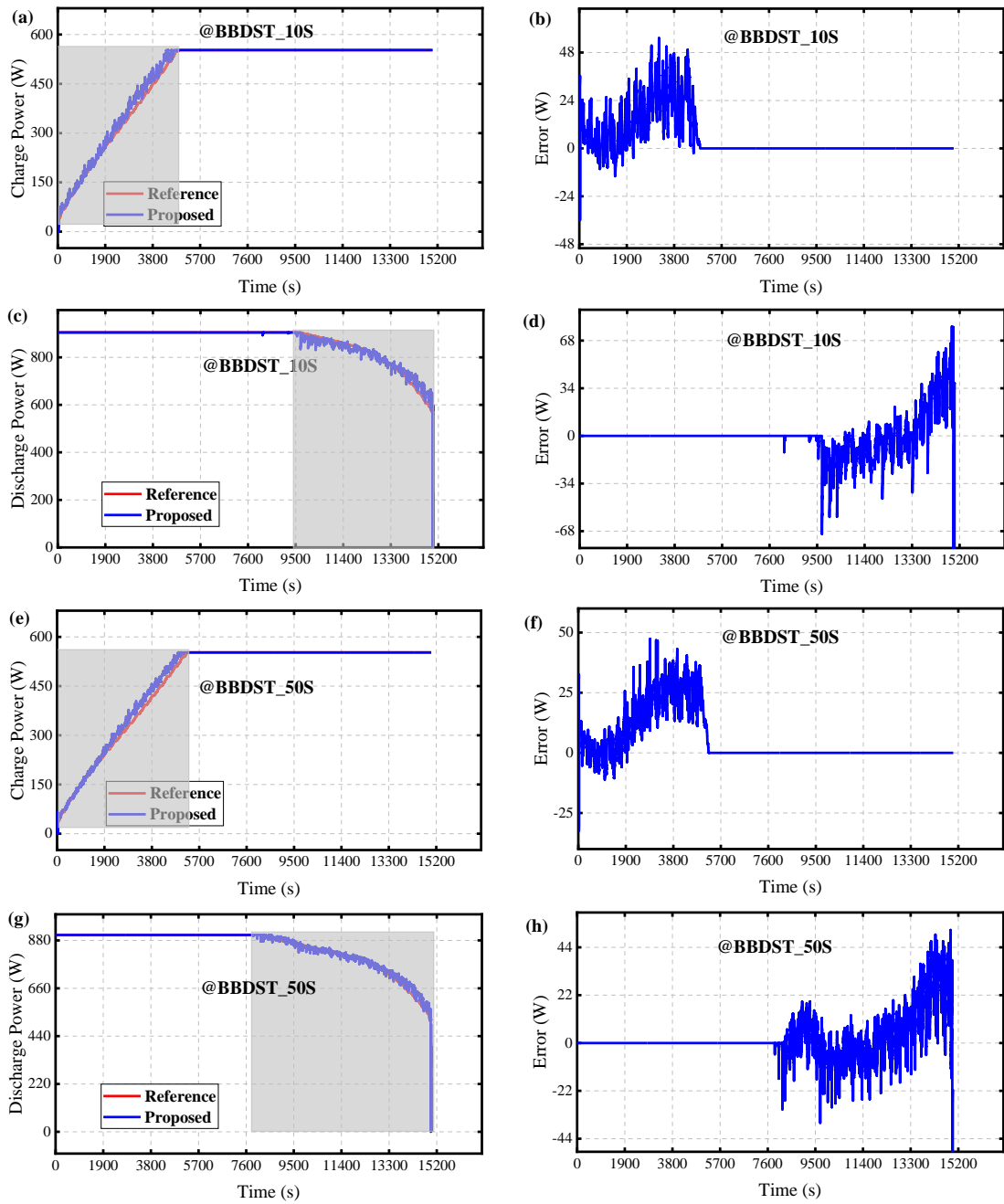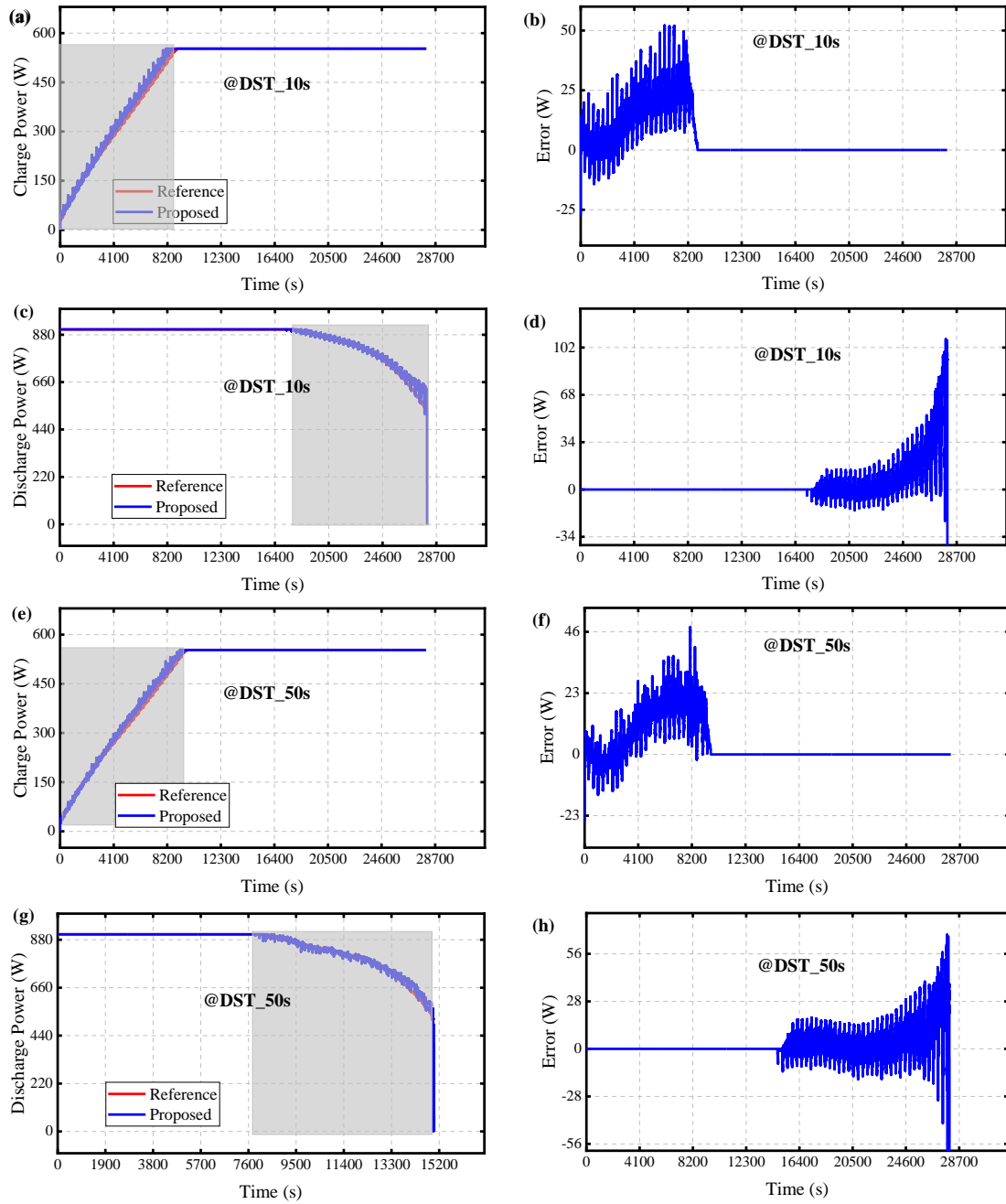
Figure 10. Peak power prediction results under BBDST conditions: (a) Charge peak power prediction at *L*=10s; (b) Charge peak power prediction error at *L*=10s; (c) Discharge peak power prediction at *L*=10s; (d) Discharge peak power prediction error at *L*=10s; (e) Charge peak power prediction at *L*=50s; (f) Charge peak power prediction error at *L*=50s; (g) Discharge peak power prediction at *L*=50s; (h) Discharge peak power prediction error at *L*=50s;

Figure 10. Peak power prediction results under DST conditions: (a) Charge peak power prediction at *L*=10s; (b) Charge peak power prediction error at *L*=10s; (c) Discharge peak power prediction at *L*=10s; (d) Discharge peak power prediction error at *L*=10s; (e) Charge peak power prediction at *L*=50s; (f) Charge peak power prediction error at *L*=50s; (g) Discharge peak power prediction at *L*=50s; (h) Discharge peak power prediction error at *L*=50s;

3.5 Analysis and discussion of peak power prediction at different temperatures

The temperature environment has a strong influence on the internal parameters of the battery,

so this section analyzes and discusses the peak power of the battery at different temperatures. To analyze the effect of temperature on the internal parameters of the battery, this paper identifies the parameters of the proposed battery model for charging and discharging at different temperatures. The model parameters for the charging and discharging stages at different temperatures are shown in Figure 12.
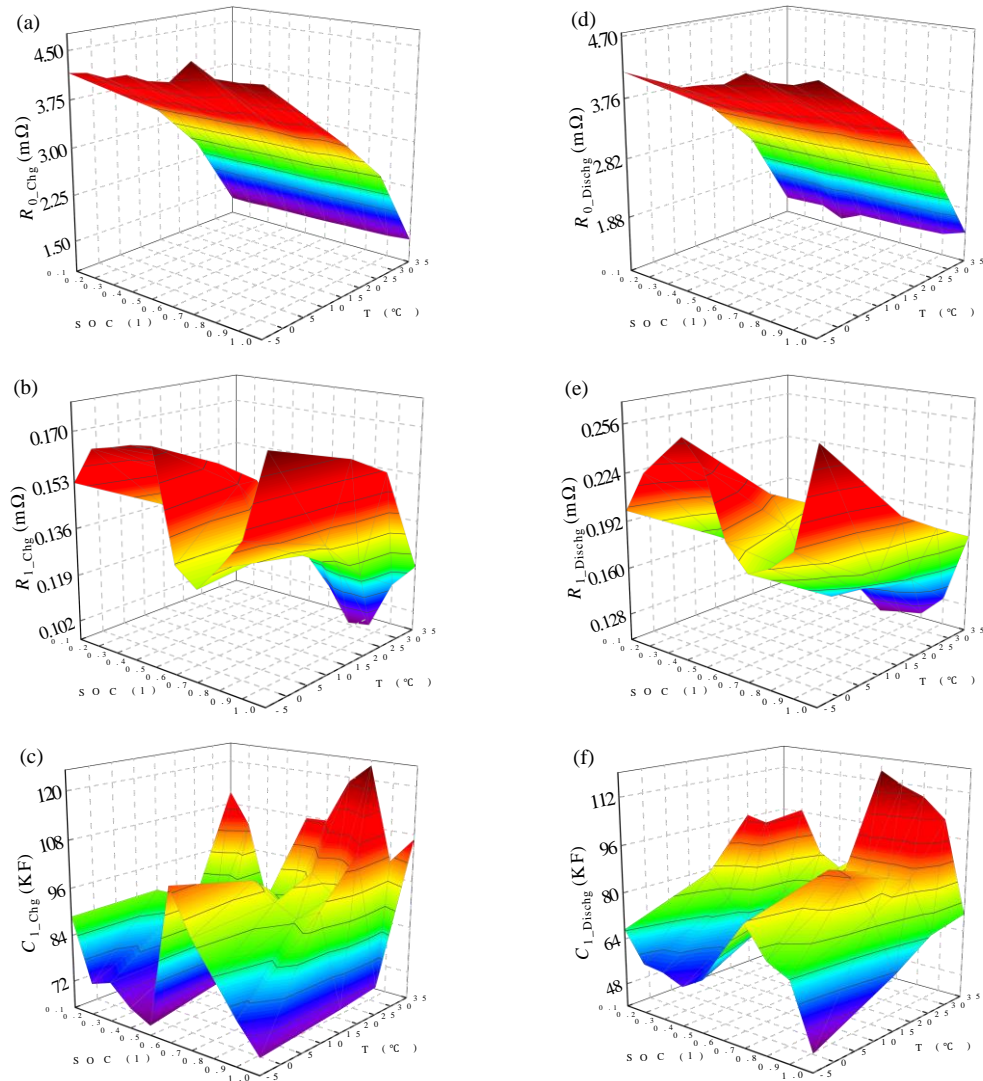

Figure 12. ECM parameters for charge and discharge phases at different temperatures: (a) Ohmic internal resistance R_0 at a charge; (b) Polarized internal resistance R_1 at a charge; (c) Polarized internal capacitance C_1 at a charge; (d) Ohmic internal resistance R_0 at discharge; (e) Polarized internal resistance R_1 at discharge; (f) Polarized internal capacitance C_1 at discharge;

From Figure 12, it can be analyzed that the battery ambient temperature has a significant effect on the operating characteristics of the LIB, especially under extreme operating temperature conditions, the operating characteristics of the LIB will change significantly with

high and low-temperature operating characteristics. The influence of temperature on the parameters is obvious and the trend is similar whether the battery is in the charging process or the discharge process. The LIB will swell inside the battery in a 35°C operating environment, and the corresponding internal electrolyte concentration will decrease. At this time, the movement rate of lithium ions in the electrolyte will slow down, while increasing the polarization of the battery. The internal resistance of the battery itself is only milliohm (mΩ) level, and as the temperature increases it can be seen that the internal resistance of the battery tends to decrease, indicating that the LIB has better performance at high temperatures within a certain range. The smaller the resistance, the less power it consumes through the current. Therefore, the battery can put out more energy and produce more peak battery power under the same environmental conditions.

To better analyze the effect of ambient temperature on the peak power of the battery, four temperature points of -5°C, 15°C, 25°C and 35°C are selected for testing and comparison. The sustained peak power capability at different temperatures for different operating conditions with a sampling interval of 10s is shown in Figure 13.

The results can be derived from Figure 13, where it can be found that the continuous discharge and charge peak power and current, increase with the temperature. The results are similar for BBDST and DST conditions, which are mainly due to the variation of ohmic internal resistance at different temperatures. When the temperature increases, the ohmic resistance of the battery decreases, the current increases, and therefore the power capacity increases accordingly.

From the above results, two analyses are derived for the effect of temperature in this paper. In the case of extreme temperatures (less than -5°C), the error of the battery model will be large, and the accuracy of the power prediction is low at this time. As the battery model error will lead to SOC estimation error, it indirectly leads to OCV error, which is placed in inaccurate parameter identification, thus leading to inaccurate Direct Current (DC) internal resistance R_0 and thus inaccurate peak power prediction. When the temperature is high, despite the higher power calculated by the model, high-power charging and discharging can easily lead to a high-temperature rise of the battery and cause safety hazards. Thus, it is also necessary to make certain limits on the power. However, the BMS leads to less power under actual high-

temperature conditions. Therefore, accurate prediction of battery temperature can improve the adaptability of the BMS.
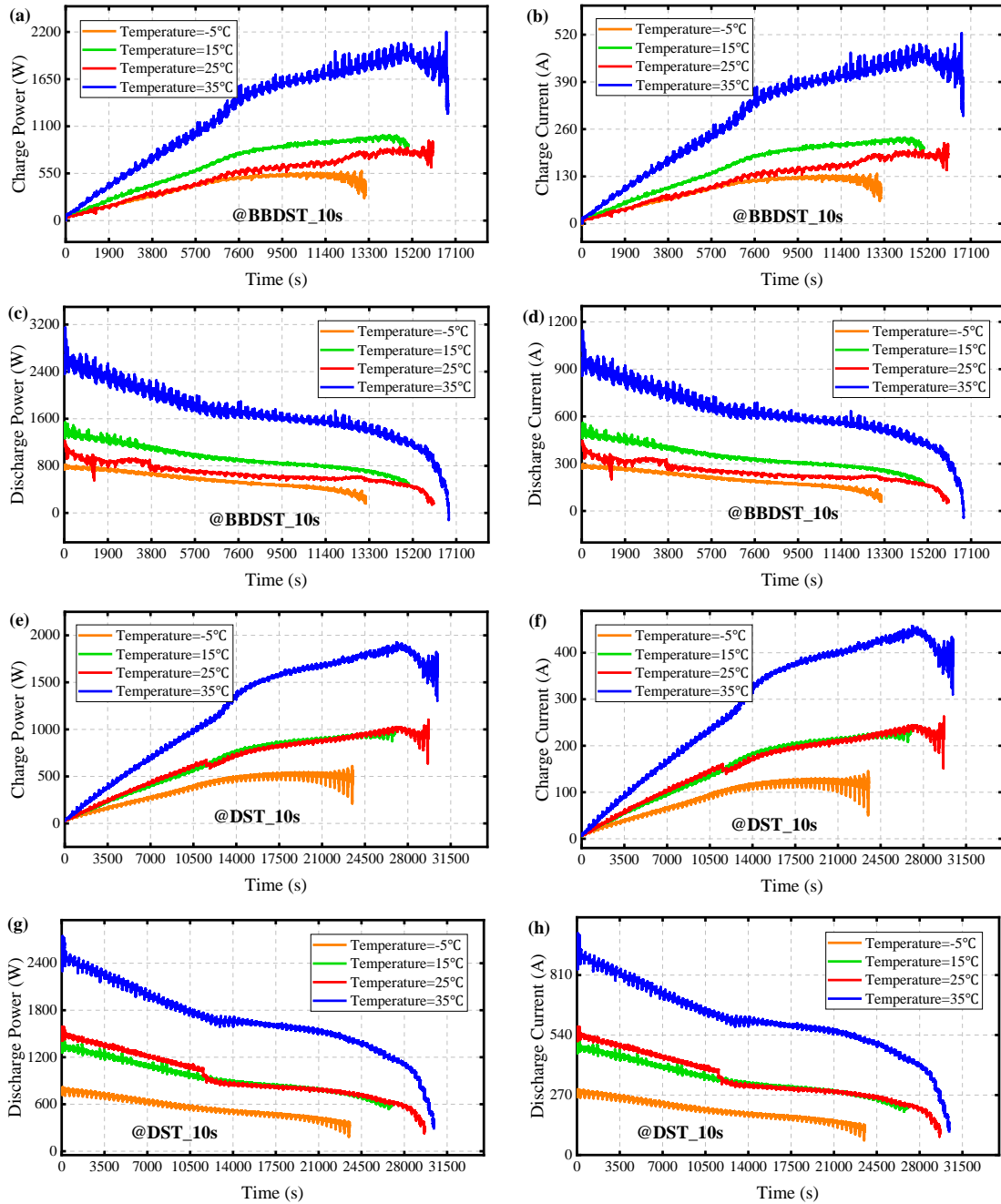

Figure 13. Peak power of different conditions at different temperatures: (a) Charge peak power at BBDST condition; (b) Charge current at BBDST condition; (c) Discharge peak power at BBDST condition; (d) Discharge current at BBDST condition; (e) Charge peak power at DST condition; (f) Charge current at DST condition; (g) Peak discharge power under DST condition; (h) Discharge current under DST condition;

4 Conclusions

Battery state of charge and peak power state prediction can not only provide new solutions for battery power optimization but also guarantee safe, reliable, and long-lasting battery operation. To accurately predict the peak battery power, a multi-parameter constrained dynamic adaptive observer considering the hysteresis characteristics and current measurement deviation correction is proposed in this paper to predict the state of charge and peak power of the lithium-ion batteries. The following conclusions were drawn from different complex dynamic tests:

(1) The proposed high-fidelity Thevenin model, which considers the battery polarization and hysteresis phenomena, enables accurate characterization of the external battery properties by approximating the high degree of nonlinearity of the battery.

(2) The proposed strategy is based on the double-layer forgetting factor recursive least squares algorithm for current measurement deviation correction to reduce the impact of current measurement deviation on modeling and state estimation. The algorithm is validated for the Beijing bus dynamic stress test and dynamic stress test conditions, and the accuracy of model parameter identification and current measurement deviation correction is better.

(3) The proposed adaptive dynamic state observer solves the problem of nonlinearity and noise interference in battery system state estimation. This method can accurately and quickly predict the state of charge at multiple temperatures and the peak power at different time scales.

(4) Temperature variation is one of the main factors affecting the peak power of the battery, and accurate prediction of the battery temperature can improve the adaptability of the battery management systems. In the future, we will continue to improve the real-time performance of the prediction algorithm and carry out peak power evaluation based on battery extreme temperature variation constraints.

Acknowledgments

References

［1］Xiao, CW et al. Comprehensive investigation on Lithium batteries for electric and hybrid-electric unmanned aerial vehicle applications. Thermal Science and Engineering Progress, 2023; 38: 101167.

［2］Wang, YJ et al. A comprehensive review of battery modeling and state estimation approaches for advanced battery management systems. Renewable & Sustainable Energy Reviews, 2020; 131: 110015.

［3］Shi, HT et al. Improved multi-time scale lumped thermoelectric coupling modeling and parameter dispersion evaluation of lithium-ion batteries. Applied Energy, 2022; 324: 119789.

［4］Li, K et al. A novel Co-estimation framework of state-of-charge, state-of-power and capacity for lithium-ion batteries using multi-parameters fusion method. Energy, 2023; 269: 126820.

［5］Wang, YJ et al. Power capability evaluation for lithium iron phosphate batteries based on multi-parameter constraints estimation. Journal of Power Sources, 2018; 374: 12-23.

［6］Qi, CS et al. A Novel Multi-Constraint Peak Power Prediction Method Combined with Online Model Parameter Identification and State-of-Charge Co-Estimation of Lithium-Ion Batteries. Journal of the Electrochemical Society, 2023; 169(12): 120505.

［7］Hu, XS et al. State estimation for advanced battery management: Key challenges and future trends. Renewable & Sustainable Energy Reviews, 2019; 114: 109334.

［8］Shrivastava, P et al. Review on technological advancement of lithium-ion battery states estimation methods for electric vehicle applications. Journal of Energy Storage, 2023; 64: 107159.

［9］Liu, CH et al. State of power estimation of lithium-ion battery based on fractional-order equivalent circuit model. Journal of Energy Storage, 2021; 41: 102954.

［10］Tang, XP et al. Model migration based battery power capability evaluation considering uncertainties of temperature and aging. Journal of Power Sources, 2019; 440: 227141.

［11］Wu, HF et al. An investigation on electrical and thermal characteristics of cylindrical lithium-ion batteries at low temperatures. Energy,2021; 225: 120223.

［12］Qi, CS et al. On-Line Multi-Time Scale Adaptive Parameter Identification Based on Improved

Lithium-Ion Batteries Hysteresis Characteristic-Electrical Equivalent Circuit Modeling. Journal of the Electrochemical Society, 2023; 170(4): 040532.

[13] Wang, SL et al. Review-Optimized Particle Filtering Strategies for High-Accuracy State of Charge Estimation of LIBs. Journal of The Electrochemical Society, 2023; 170(5): 050514.

[14] Li, R et al. Research on Multi-Time Scale SOP Estimation of Lithium-Ion Battery Based on H8 Filter. Batteries-Basel, 2023; 9(4): 191.

[15] Seo, M et al. Innovative lumped-battery model for state of charge estimation of lithium-ion batteries under various ambient temperatures. Energy, 2021; 226: 120301.

[16] Yu, P et al. Study of hysteresis voltage state dependence in lithium-ion battery and a novel asymmetric hysteresis modeling. Journal of Energy Storage, 2022; 51: 104492.

[17] Sun, CC et al. Improved parameter identification and state-of-charge estimation for lithium-ion battery with fixed memory recursive least squares and sigma-point Kalman filter. Electrochimica Acta, 2021; 387: 138501.

[18] Xie, SY et al. State-of-Charge Estimation of Lithium-Ion Battery Based on an Improved Dual-Polarization Model. Energy Technology, 2023; 11(4).

[19] Axen, JB et al. Evaluation of hysteresis expressions in a lumped voltage prediction model of a NiMH battery system in stationary storage applications. Journal of Energy Storage, 2022; 48: 103985.

[20] Shi, HT et al. A novel lumped thermal characteristic modeling strategy for the online adaptive temperature and parameter co-estimation of vehicle lithium-ion batteries. Journal of Energy Storage, 2022; 50: 104309.

[21] Tian, JQ et al. Lithium-ion battery health estimation with real-world data for electric vehicles. Energy, 2023; 270: 126855.

[22] Ul Hassan, M et al. A comprehensive review of battery state of charge estimation techniques. Sustainable Energy Technologies and Assessments, 2022; 54: 102801.

[23] Naseri, F et al. An Enhanced Equivalent Circuit Model With Real-Time Parameter Identification for Battery State-of-Charge Estimation. IEEE Transactions on Industrial Electronics, 2022; 69(4): 3743-3751.

[24] Knap, V et al. Effects of open-circuit voltage tests and models on state-of-charge estimation for batteries in highly variable temperature environments: Study case nano-satellites. Journal of

Power Sources, 2021; 498: 229913.

[25] Wu, CL et al. State-of-charge estimation of lithium-ion batteries based on MCC-AEKF in non-Gaussian noise environment. Energy, 2023; 274: 127316.

[26] Chen, LP et al. Adaptive state-of-charge estimation of lithium-ion batteries based on square-root unscented Kalman filter. Energy, 2022; 252: 123972.

[27] Zhang, WG et al. Adaptive unscented Kalman filter based state of energy and power capability estimation approach for lithium-ion battery. Journal of Power Sources, 2015; 289: 50-62.

[28] Liu, CH et al. State of power estimation of lithium-ion battery based on fractional-order equivalent circuit model. Journal of Energy Storage, 2021; 41: 102954.

[29] Wei, ZB et al. Noise-Immune Model Identification and State-of-Charge Estimation for Lithium-Ion Battery Using Bilinear Parameterization. IEEE Transactions on Industrial Electronics, 2021; 68(1): 312-323.

[30] Zheng, YJ et al. Investigating the error sources of the online state of charge estimation methods for lithium-ion batteries in electric vehicles. Journal of Power Sources, 2018; 377: 161-188

[31] He, JT et al. Two-layer online state-of-charge estimation of lithium-ion battery with current sensor bias correction. International Journal of Energy Research, 2019; 43 (8): 3837-3852.

[32] Tang, XP et al. A method for state-of-charge estimation of LiFePO4 batteries based on a dual-circuit state observer. Journal of Power Sources, 2015; 296: 23-29.

[33] Wu, TT et al. Research on electrochemical characteristics and heat generating properties of power battery based on multi-time scales. Energy, 2023; 265: 126416.

[34] Yang, X et al. A novel fuzzy adaptive cubature Kalman filtering method for the state of charge and state of energy co-estimation of lithium-ion batteries. Electrochimica Acta, 2022; 415: 140241.

[35] Li, BW et al. A linear recursive state of power estimation method based on fusion model of voltage and state of charge limitations. Journal of Energy Storage, 2021; 40: 102583.

[36] Cui, ZH et al. A combined state-of-charge estimation method for lithium-ion battery using an improved BGRU network and UKF. Energy, 2022; 259: 124933.

[37] Zhang, SZ et al. State-of-charge estimation for lithium-ion battery during constant current charging process based on model parameters updated periodically. Energy, 2022; 257: 124770.

[38] Sheng, C et al. Energy management strategy based on health state for a PEMFC/Lithium-ion batteries hybrid power system. Energy Conversion and Management, 2022; 271: 116330.

［39］Jiang, C et al. A state-of-charge estimation method of the power lithium-ion battery in complex conditions based on adaptive square root extended Kalman filter. Energy, 2021; 219: 119603.